CHAPTER 1

MODELING DYNAMIC FRACTURE USING LARGE-SCALE ATOMISTIC SIMULATIONS

Markus J. Buehler

Massachusetts Institute of Technology,
Department of Civil and Environmental Engineering
77 Massachusetts Avenue Room 1-272, Cambridge, MA., 02139, USA
E-mail: mbuehler@MIT.EDU

Huajian Gao

Max Planck Institute for Metals Research
Heisenbergstrasse 3, D-70569 Stuttgart, Germany

We review a series of large-scale molecular dynamics studies of dynamic fracture in brittle materials, aiming to clarify questions such as the limiting speed of cracks, crack tip instabilities and crack dynamics at interfaces. This chapter includes a brief introduction of atomistic modeling techniques and a short review of important continuum mechanics concepts of fracture. We find that hyperelasticity, the elasticity of large strains, can play a governing role in dynamic fracture. In particular, hyperelastic deformation near a crack tip provides explanations for a number of phenomena including the "mirror-mist-hackle" instability widely observed in experiments as well as supersonic crack propagation in elastically stiffening materials. We also find that crack propagation along interfaces between dissimilar materials can be dramatically different from that in homogeneous materials, exhibiting various discontinuous transition mechanisms (mother-daughter and mother-daughter-granddaughter) to different admissible velocity regimes.

1. Introduction

Why and how cracks spread in brittle materials is of essential interest to numerous scientific disciplines and technological applications [1-3]. Large-scale molecular dynamics (MD) simulation [4-13] is becoming an increasingly useful tool to investigate some of the most fundamental aspects of dynamic fracture [14-20]. Studying rapidly propagating cracks using atomistic methods is particularly attractive, because cracks propagate at speeds of kilometers per second, corresponding to time-and length scales of nanometers per picoseconds readily accessible within classical MD methods. This similarity in time and length scales partly explains the success of MD in describing the physics and mechanics of dynamic fracture.

1.1 Brief review: MD modeling of fracture

Atomistic simulations of fracture were carried out as early as 1976, in first studies by Ashurst and Hoover [21]. Some important features of dynamic fracture were described in that paper, although the simulation sizes were extremely small, comprising of only 64x16 atoms with crack lengths around ten atoms. A later classical paper by Abraham and coworkers published in 1994 stimulated much further research in this field [22]. Abraham and coworkers reported molecular-dynamics simulations of fracture in systems up to 500,000 atoms, which was a significant number at the time. In these atomistic calculations, a Lennard-Jones (LJ) potential [23] was used. The results in [22, 24] were quite striking because the molecular-dynamics simulations were shown to reproduce phenomena that were discovered in experiments only a few years earlier [25]. An important classical phenomenon in dynamic fracture was the so-called “mirror-mist-hackle” transition. It was known since 1930s that the crack face morphology changes as the crack speed increases. This phenomenon is also referred to as dynamic instability of cracks. Up to a speed of about one third of the Rayleigh-wave speed, the crack surface is atomically flat (mirror regime). For higher crack speeds the crack starts to roughen (mist regime) and eventually becomes very rough (hackle regime), accompanied by extensive crack branching and

perhaps severe plastic deformation near the macroscopic crack tip. Such phenomena were observed at similar velocities in both experiments and modeling [25]. Since the molecular-dynamics simulations are performed in atomically perfect lattices, it was concluded that the dynamic instabilities are a universal property of cracks, which have been subject to numerous further studies in the following years (e.g. [26]).

The last few years have witnessed ultra large-scale atomistic modeling of dynamical fracture with system sizes exceeding one billion atoms [4, 5, 12, 13, 27, 28]. Many aspects of fracture have been investigated, including crack limiting speed [10, 29-31], dynamic fracture toughness [32] and dislocation emission processes at crack tips and during nanoindentation [33, 34]. Recent progresses also include systematic atomistic-continuum studies of fracture [29-31, 35-38], investigations of the role of hyperelasticity in dynamic fracture [30, 39] and the instability dynamics of cracks [22, 24, 39]. A variety of numerical models have been proposed, including concurrent multi-scale schemes that combine atomistic and continuum domains within a single model [40-48].

1.2 Outline of this chapter

In this chapter, we mainly focus on the work involved by the authors in using simplistic interatomic potentials to probe crack dynamics in model materials, with an aim to gain broad insights into fundamental, physical aspects of dynamic fracture.

A particular focus of our studies is on understanding the effect of hyperelasticity on dynamic fracture. Most existing theories of fracture assume a linear elastic stress–strain law. However, the relation between stress and strain in real solids is strongly nonlinear due to large deformations near a moving crack tip, a phenomenon referred to here as hyperelasticity. Our studies strongly suggest that hyperelasticity, in contrast to most of the classical linear theories of fracture, indeed has a major impact on crack dynamics.

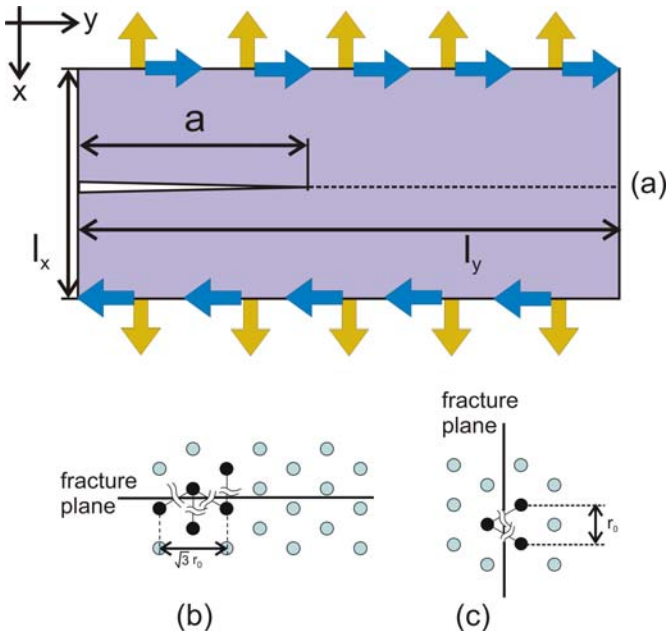

Fig. 1. Subplot (a): A schematic illustration of the simulation geometry used in our large-scale atomistic studies of fracture. The geometry is characterized by the slab width l_x and slab length l_y, and the initial crack length a. We consider different loading cases, including mode I, mode II (indicated in the figure) and mode III (not shown). Subplots (b) and (c) illustrate two different possible crack orientations. Configuration (b) is used for the studies discussed in Sections 3 and 5, whereas configuration (c) is used for the studies described in Section 4. The orientation shown in subplot (c) has lower fracture surface energy than the orientation shown in subplot (b).

The plan of this chapter is as follows. First, we review atomistic modeling techniques, in particular our approach of using simple model potentials to study dynamic fracture. We will then cover three topics: (i) confined crack dynamics along weak layers in homogeneous materials, focusing on the crack limiting speed (Section 3), (ii) instability dynamics of fracture, focusing on the critical speed for the onset of crack instability (Section 4), and (iii) dynamics of cracks at interfaces of dissimilar materials (Section 5). Whereas cracks are confined to propagate along a

prescribed path in Section 3, they are completely unconstrained in Section 4. Section 5 contains studies on both constrained and unconstrained crack propagation. We conclude with a discussion and outlook to future research in this area.

2. Large-scale atomistic modeling of dynamic fracture: A fundamental viewpoint

2.1 Molecular dynamics simulations

Our simulation tool is classical molecular-dynamics (MD) [23, 49]. For a more thorough review of MD and implementation on supercomputers, we refer the reader to other articles and books [19, 23, 50-52]. Here we only present a very brief review. MD predicts the motion of a large number of atoms governed by their mutual interatomic interaction, and it requires numerical integration of Newton's equations of motion usually via a Velocity Verlet algorithm [23] with time step Δt on the order of a few femtoseconds.

2.2 Model potentials for brittle materials: A simplistic but powerful approach

The most critical input parameter in MD is the choice of interatomic potentials [23, 49]. In the studies reported in this article, the objective is to develop an interatomic potential that yields generic elastic behaviors at small and large strains, which can then be linked empirically to the behavior of real materials and allows independent variation of parameters governing small-strain and large-strain properties. Interatomic potentials for a variety of different brittle materials exist, many of which are derived form first principles (see, for example [53-55]). However, it is difficult to identify generic relationships between potential parameters and macroscopic observables such as the crack limiting or instability speeds when using such complicated potentials. We deliberately avoid these complexities by adopting a simple pair potential based on a harmonic interatomic potential with spring constant

k_0. In this case, the interatomic potential between pairs of atoms is expressed as

$$\phi(r) = a_0 + \frac{1}{2} k_0 \left(r - r_0\right)^2, \tag{1}$$

where r_0 denotes the equilibrium distance between atoms, for a 2D triangular lattice, as schematically shown in the inlay of Figure 1. This harmonic potential is a first-order approximation of the Lennard-Jones 12:6 potential [23], one of the simplest and most widely used pair potentials defined as

$$\phi(r) = 4\varepsilon\left(\left[\frac{\sigma}{r}\right]^{12} - \left[\frac{\sigma}{r}\right]^{6}\right). \tag{2}$$

We express all quantities in reduced units, so that lengths are scaled by the LJ-parameter σ which is assumed to be unity, and energies are scaled by the parameter ε, the depth of the minimum of the LJ potential. We note that corresponding to choosing $\varepsilon = 1$ in eq. (2), we choose $a_0 = -1$ in the harmonic approximation shown in eq. (1). Further, we note that $r_0 = \sqrt[6]{2} \approx 1.12246$ (see Figure 1). Note that the parameter σ is coupled to the lattice constant a as $\sigma = a / \sqrt{2} / \sqrt[6]{2}$. The reduced temperature is $\mathrm{k}_B T / \varepsilon$ with k_B being the Boltzmann constant. The mass of each atoms in the models is assumed to be unity, relative to the reference mass m^*. The reference time unit is then given by $t^* = \sqrt{m^* \sigma^2 / \varepsilon}$. For example, when choosing electron volt as reference energy ($\varepsilon = 1$ eV), Angstrom as reference length ($\sigma = 1$ Å), and the atomic mass unit as reference mass ($m^* = 1$ amu), the reference time unit corresponds to $t^* \approx 1.01805\mathrm{E}\text{-}14$ seconds.

Although the choice of a simple harmonic interatomic potential can not lead to quantitative calculations of fracture properties in a particular material, it allows us to draw certain generic conclusions about fundamental, material-independent mechanisms that can help elucidating the physical foundations of brittle fracture. The harmonic potential leads to linear elastic material properties, and thus serves as the starting point when comparing simulation results to predictions by the classical linear theories of fracture.

Various flavors and modifications of the simplistic, harmonic model potentials as described in eq. (1) are used for the studies reviewed in this article. These modifications are discussed in detail in each section. The concept of using simplistic model potentials to understand the generic features of fracture was pioneered by Abraham and coworkers [10, 12, 22, 24, 31, 40, 56-58].

2.3 Model geometry and simulation procedure

We typically consider a crack in a two-dimensional geometry with slab size $l_x \times l_y$ and initial crack length a, as schematically shown in Fig. 1. The slab size is chosen large enough such that waves reflected from the boundary do not interfere with the propagating crack at early stages of the simulation. The slab size in the crack direction is chosen between 2 and 4 times larger than the size orthogonal to the initial crack.

The slab is initialized at zero temperature prior to simulation. Most of our studies are carried out in a two-dimensional, hexagonal lattice. The three-dimensional studies are performed in a FCC lattice, with periodic boundary conditions in the out-of-plane *z* direction.

The slab is slowly loaded with a constant strain rate of $\dot{\varepsilon}_x$ (corresponding to tensile, mode I loading), and/or $\dot{\varepsilon}_{xy}$ (corresponding to shear, mode II loading). We establish a linear velocity gradient prior to simulation to avoid shock wave generation from the boundaries. While the loading is applied, the stress σ_{ij} (corresponding to the specified loading case) steadily increases leading to a slowly increasing crack velocity upon fracture initiation. In the case of anti-plane shear loading (mode III), the load is applied in a similar way. It can be shown that the stress intensity factor remains constant in a strip geometry inside a region of crack lengths a [59]

$$\tfrac{1}{4} l_x < a < (l_y - \tfrac{1}{4} l_x). \tag{3}$$

Accurate determination of crack tip velocity is crucial as we need to be able to measure small changes in the propagation speed. The crack tip position a is determined by finding the surface atom with maximum y position in the interior of a search region inside the slab using a potential energy criterion. This quantity is averaged over small time

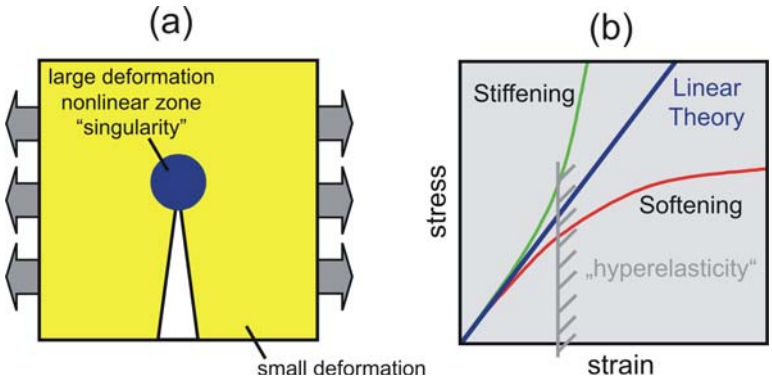

Fig. 2. The concept of hyperelasticity (a) and the region of large deformation near a moving crack (b). The linear elastic approximation is only valid for small deformation. Close to crack tips, material deformation is extremely large, leading to significant changes of local elasticity, referred to as "hyperelasticity". Our research results show that this local elasticity can, under certain conditions, completely govern the dynamics of fracture, in which case the assumption of linear elastic material behavior becomes insufficient to describe the physics of fracture [30, 60, 61].

intervals to eliminate very high frequency fluctuations. To obtain the steady state velocity of the crack, crack speed measurements are performed within a region of constant stress intensity factor.

3. Constrained cracks in homogeneous materials: How fast can cracks propagate?

In this section we focus on the limiting speed of cracks, discussing recent results on cracks faster than both shear and longitudinal wave speeds in an elastically stiffening material [10, 12, 30, 31].

The elasticity of a solid clearly depends on its state of deformation. Metals will weaken, or soften, and polymers may stiffen as the strain approaches the state of materials failure. It is only for infinitesimal deformation that the elastic moduli can be considered constant and the elasticity of the solid linear. However, many existing theories model fracture using linear elasticity. Certainly, this can be considered questionable since material is failing at the tip of a dynamic crack

because of the extreme deformation there. Here we show by large-scale atomistic simulations that hyperelasticity, the elasticity of large strains, can play a governing role in the dynamics of fracture. We introduce the concept of a characteristic length scale χ for the energy flux near the crack tip and demonstrate that the local hyperelastic wave speed governs the crack speed when the hyperelastic zone approaches this energy length scale χ [30].

3.1 Introduction: The limiting speed of cracks

We show by large-scale atomistic simulation that hyperelasticity, the elasticity of large strains, can play a governing role in the dynamics of brittle fracture [30, 62, 63]. This is in contrast to many existing theories of dynamic fracture where the linear elastic behavior of solids is assumed sufficient to predict materials failure [14]. Real solids have elastic properties that are significantly different for small and for large deformations. The concept of hyperelasticity, both for stiffening and softening material behavior, is reviewed in Figure 2, indicating the region close to a moving crack where hyperelastic material behavior is important.

A number of phenomena associated with rapidly propagating cracks are not thoroughly understood. Some experiments [25, 64] and computer simulations [22, 24] have shown a significantly reduced crack propagation speed in comparison with the predictions by the theory. In contrast, other experiments indicated that over 90% of the Rayleigh wave speed can be achieved [65]. Such discrepancies between theories, experiment and simulations cannot always be attributed to the fact that real solids have many different types of imperfections, such as grain boundaries and microcracks (either pre-existing or created during the crack propagation), as similar discrepancies also appear in molecular-dynamics simulations of cracks traveling in perfect atomic lattices.

Gao [62, 63] and Abraham [22, 24, 56] have independently proposed that hyperelastic effects at the crack tip may play an important role in the dynamics of fracture. Their suggestions have been used to help to explain phenomena related to crack branching and dynamic crack tip instability, as well as explaining the significantly lower maximum crack propagation

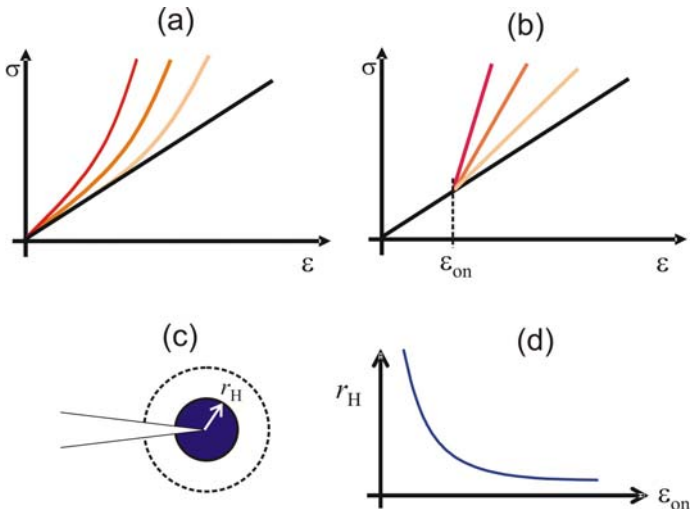

Fig. 3. Concept of increasingly strong hyperelastic effect (subplot (a)). The increasingly strong hyperelastic effect is modeled by using biharmonic potentials (subplot (b)). The bilinear or biharmonic model allows to tune the size of the hyperelastic region near a moving crack, as indicated in subplots (c) and (d) [30]. The local increase of elastic modulus and thus wave speeds can be tuned by changing the slope of the large-strain stress-strain curve ("local modulus" [30, 62, 63]).

speed observed in some experiments and many computer simulations. However, it is not generally accepted that hyperelasticity should play a significant role in dynamic fracture. One reason for this belief stems from the fact that the zone of large deformation in a loaded body with a crack is highly confined to the crack tip, so that the region where linear elastic theory does not hold is extremely small compared to the extensions of the specimen [14, 15]. This is demonstrated in Figure 2(a).

We have performed large-scale molecular-dynamics studies in conjunction with continuum mechanics concepts to demonstrate that hyperelasticity can be crucial for understanding dynamic fracture. Our study shows that local hyperelasticity around the crack tip can significantly influence the limiting speed of cracks by enhancing or reducing local energy flow. This is true even if the zone of hyperelasticity is small compared to the specimen dimensions. The hyperelastic theory completely changes the concept of the maximum

crack velocity in the classical theories. For example, the classical theories [14, 15] clearly predict that mode I cracks are limited by the Rayleigh wave speed and mode II cracks are limited by the longitudinal wave speed. In mode III, theory predicts that the limiting speed of cracks is the shear wave speed [14, 15]. In contrast, super-Rayleigh mode I and supersonic mode II cracks are allowed by hyperelasticity and have been seen in computer simulations [13, 31]. We have also observed mode III cracks faster than the shear wave speed [66].

3.2 Strategy of investigation

Our strategy of study is to first establish harmonic reference systems with behaviors perfectly matching those predicted by the existing linear elastic theories of fracture. Using a biharmonic model potentials [30], we then introduce increasingly stronger nonlinearities and show that under certain conditions, the linear elastic theory breaks down as the material behaviour near crack tips deviates increasingly from the linear elastic approximation. This is further visualized in Figure 3.

In comparison with experiments, a major advantage of computer simulations is that they allow material behaviors to be fine tuned by introducing interatomic potentials that focus on specific aspects, one at a time, such as the large-strain elastic modulus, smoothing at bond breaking and cohesive stress. From this point of view, MD simulations can be regarded as computer experiments that are capable of testing theoretical concepts and identifying controlling factors in complex systems.

3.3 Elastic properties: The link between the atomistic scale and continuum theory

3.3.1 The virial stress and strain

Stresses are calculated according to the virial theorem [67, 68]. The atomistic stress is given by (note that Ω is the atomic volume)

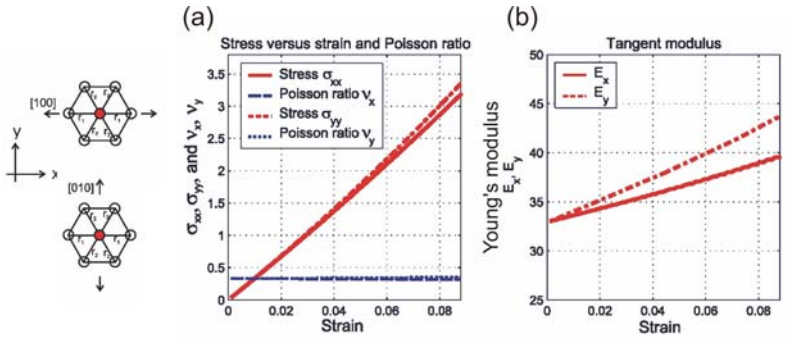

Fig. 4. Elastic properties of the two-dimensional model system with harmonic potential, including (a) stress versus strain and Poisson's ratio, and (b) tangent Young's modulus as a function of strain. The figure shows the results for two different crystal orientations (see left part of the figure) [70].

$$\sigma_{ij} = \frac{1}{\Omega}\left(\frac{1}{2}\left[\sum_{\alpha,\beta} -\frac{1}{r}\frac{\partial \phi}{\partial r} r_i r_j \Big|_{r=r_{\alpha\beta}} \right] \right). \tag{4}$$

We also use the concept of an atomic strain to link the atomistic simulation results with continuum theory. For a 2D triangular lattice, we define the left Cauchy-Green strain tensor of an atom l [69]

$$b_{ij}^{l} = \left\{ \frac{1}{3r_0^2} \sum_{k=1}^{N} \left[\left(x_i^l - x_i^k \right) \left(x_j^l - x_j^k \right) \right] \right\}, \tag{5}$$

with $N = 6$ nearest neighbors, and the variable x_i^l denoting the position vector of atom l. Unlike the virial stress, the virial strain is valid instantaneously in space and time. The maximum principal strain b_1 is obtained by diagonalization of the strain tensor b_{ij}. The maximum principal engineering strain is then given by $\varepsilon_1 = \sqrt{b_1} - 1$.

The definition of atomic stress and strain allows an immediate comparison of MD results with the prediction by continuum theory, such as changes in deformation field as a function of increasing crack speed [14]. This has been discussed extensively in the literature [29, 37, 51, 60, 61, 70, 71]. Some of these results will be reviewed later.

3.3.2 Elastic properties associated with the harmonic potential: The reference systems

The simulations considered here are all carried out in a two-dimensional triangular lattice using a harmonic interatomic potential introduced in eq. (1). For a harmonic two-dimensional elastic sheet of atoms, the Young's modulus is given by

$$E = \frac{2}{\sqrt{3}} k_0 , \tag{6}$$

and the shear modulus is

$$\mu = \frac{\sqrt{3}}{4} k_0 \tag{7}$$

(see e.g., ref. [38]). The Poisson's ratio for the two-dimensional lattice is $\nu \approx 0.33$. At large strain, this two-dimensional harmonic lattice shows a slight stiffening effect. The elastic properties for the harmonic potential are shown in Figure 4, indicating that the harmonic potential leads to linear-elastic properties as assumed in many classical fracture theories [14]. We note that when $k_0 = 36/\sqrt[3]{3} \approx 28.57$, $E \approx 33$ and $\mu \approx 24$. The shear wave speed is

$$c_s = \sqrt{\frac{\mu}{\rho}} , \tag{8}$$

the longitudinal wave speed is

$$c_l = \sqrt{\frac{E}{\rho}} , \tag{9}$$

and the Rayleigh-wave speed is $c_R \approx 0.9235 \cdot c_s$, where $\rho \approx 0.9165$ is the material density in the examples considered here.

3.3.3 Elastic properties associated with the biharmonic model potential

We adopt a biharmonic, interatomic potential composed of two spring constants $k_0 = 36/\sqrt[3]{3} \approx 28.57$ and $k_1 = 2k_0$ (all quantities given are in dimensionless units), as suggested in [30].

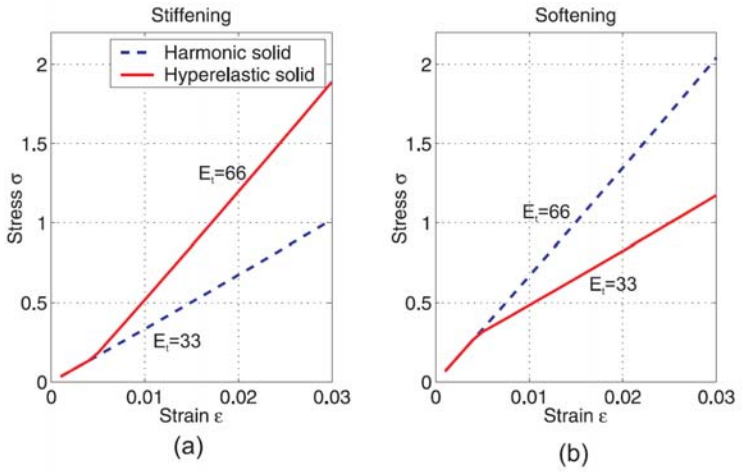

Fig. 5. Elastic properties of a triangular lattice with biharmonic interactions: stress versus strain in the *x*-direction (a) and in the *y*-direction (b). The stress state is uniaxial tension, with stress in the direction orthogonal to the loading relaxed to zero [30].

We consider two "model materials", one with elastic stiffening and the other with elastic softening behavior.

In the elastic stiffening system, the spring constant k_0 is associated with small perturbations from the equilibrium distance r_0, and the second spring constant k_1 is associated with large bond stretching for $r > r_{on}$. The role of k_0 and k_1 is reversed in the elastic softening system ($k_0 = 2k_1$, and $k_1 = 36/\sqrt[3]{3}$). Purely harmonic systems (corresponding to eq. (1)) are obtained if r_{on} is chosen to be larger than r_{break}. The interatomic potential is defined as

$$\phi(r) = \begin{cases} \frac{1}{2}k_0(r-r_0)^2 & \text{if } r < r_{on}, \\ a_2 + \frac{1}{2}k_1(r-r_1)^2 & \text{if } r \geq r_{on}. \end{cases} \tag{10}$$

The other parameters of the potential are determined to be

$$a_2 = \tfrac{1}{2}k_0(r_{on}-r_0)^2 - \tfrac{1}{2}k_1(r_{on}-r_1)^2, \tag{11}$$

and

$$r_1 = \tfrac{1}{2}(r_{on}+r_0) \tag{12}$$

from continuation conditions. The elastic properties associated with this potential are shown in Figure 5 for uniaxial stress in the *x* and *y*-directions. This potential allows to smoothly interpolate between harmonic potentials and strongly nonlinear potentials by changing the parameter r_{on} and/or the ratio of the spring constants k_1 / k_0.

3.3.4 Fracture surface energy

The fracture surface energy γ is an important quantity for nucleation and propagation of cracks. It is defined as the energy required to generate a unit distance of a pair of new surfaces (cracks can be regarded as sinks for energy, where elastic energy is converted into surface fracture energy). The Griffith criterion predicts that the crack tip begins to propagate when the crack tip energy release rate *G* reaches the fracture surface energy $G = 2\gamma$ [72]. Knowledge of the atomic lattice and the interatomic potential can also be used to define the fracture surface energy. This quantity depends on the crystallographic directions and is calculated to be

$$\gamma = -\frac{\Delta\phi}{d}, \tag{13}$$

where $\Delta\phi$ the energy necessary to break atomic bonds as the crack advances a distance d. For the harmonic bond snapping potential as described above, the fracture surface energy is given by $\gamma \approx 0.0332$ for the direction of high surface energy (Figure 1(b)), and $\gamma \approx 0.0288$ for the other direction (Figure 1(c); about 15 % smaller than in the other direction).

3.4 Harmonic reference systems

After briefly defining the atomistic models in the previous sections, we now discuss simulation results using the harmonic potentials as the reference system.

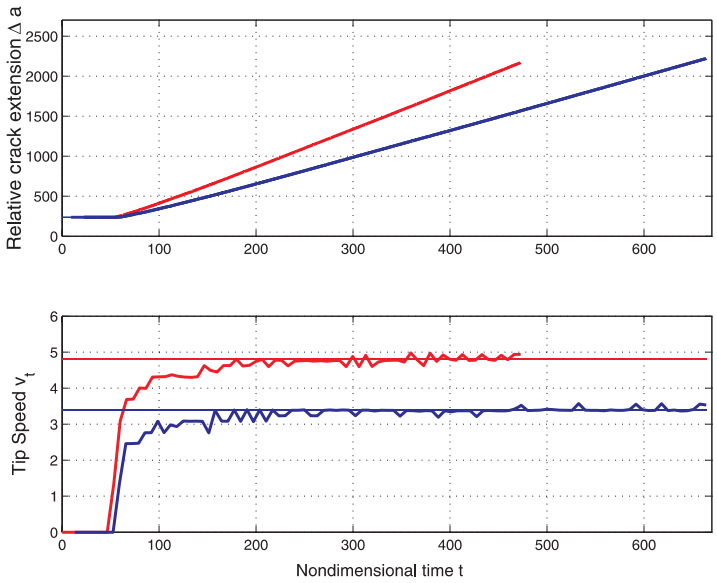

Fig. 6. Crack tip history (upper part) as well as the crack speed history (lower part) for a soft as well as a stiff harmonic material [29, 35].

Our results show that the harmonic systems behave as predicted by classical, linear elastic continuum theories of fracture [14]. For a mode I tensile crack, linear theory predicts that the energy release rate vanishes for all velocities in excess of the Rayleigh wave speed, implying that a mode I crack cannot move faster than the Rayleigh wave speed. This prediction is indeed confirmed in systems with the harmonic potential. The crack velocity approaches the Rayleigh wave speed independent of the slab size, provided that the applied strain is larger than 1.08 percent and the slab width is sufficiently large ($l_x > 1{,}000$). Results for a mode I crack and two different spring constants are shown in Figure 6.

In other studies, we find that the crack limiting speed of mode II cracks is the longitudinal wave speed. Mode III cracks are limited by the shear wave speed (details and results of those simulations are not

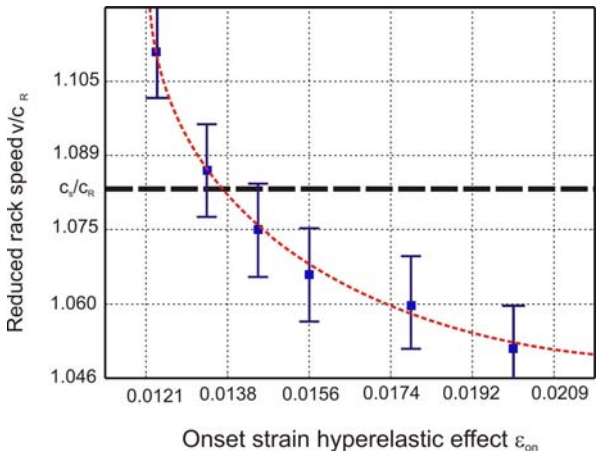

Fig. 7. Change of the crack speed as a function of ε_{on}. The smaller the ε_{on}, the larger the hyperelastic region, and the larger the crack speed [30]. These results indicate that the crack speed of mode I cracks is not limited by the Rayleigh-wave speed.

described here). These results agree well with linear elastic fracture mechanics theories [14].

3.5 Biharmonic simulations: Elastic stiffening

Now we describe a series of computer experiments carried out with the biharmonic interatomic potential introduced in eq. (4) and (5). The results indicate that a local hyperelastic zone around the crack tip (as schematically shown in Figure 2(a)) can have significant effect on the velocity of the crack.

We consider hyperelastic effect of different strengths by using a biharmonic potential with different onset strains governed by the parameter r_{on}. The parameter r_{on} governs the onset strain of the hyperelastic effect $\varepsilon_{on} = (r_{on} - r_0)/r_0$. The simulations reveal crack propagation at super-Rayleigh velocities in steady-state with a local stiffening zone around the crack tip.

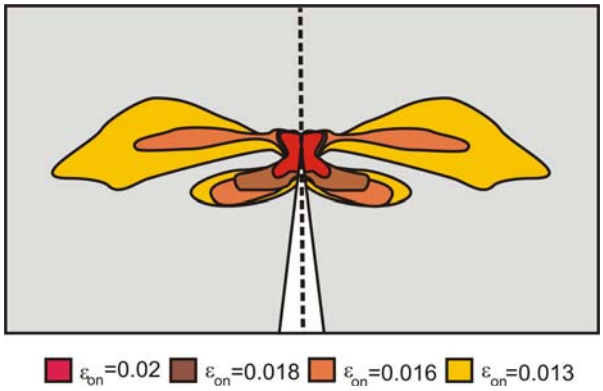

Fig. 8. Shape of the hyperelastic regions for different choices of ε_{on}. The smaller the ε_{on}, the larger the hyperelastic region. The hyperelastic region takes a complex butterfly-like shape [30].

Fig. 7 plots the crack velocity as a function of the hyperelasticity onset strain ε_{on}. We observe that the earlier the hyperelastic effect is turned on, the larger the limiting velocity. Measuring the hyperelastic area using the principal strain criterion, we find that the hyperelastic area grows as ε_{on} becomes smaller.

In Fig. 8, we depict the shape of the hyperelastic region near the crack tip for different choices of the parameter ε_{on}. The shape and size of the hyperelastic region is found to be independent of the slab width l_x. In all cases, the hyperelastic area remains confined to the crack tip and does not extend to the boundary of the simulation. The results presented in Fig. 6 show that the hyperelastic effect is sensitive to the potential parameter and the extension of the local hyperelastic zone.

Mode I cracks can travel at steady-state intersonic velocities if there exists a stiffening hyperelastic zone near the crack tip. For example, when the large-strain spring constant is chosen to be $k_1 = 4k_0$, with $r_{on} = 1.1375$ and $r_{break} = 1.1483$ (*i.e.* "stronger" stiffening and thus larger local wave speed than before), the mode I crack propagates about 20 percent faster than the Rayleigh speed of the soft material, and

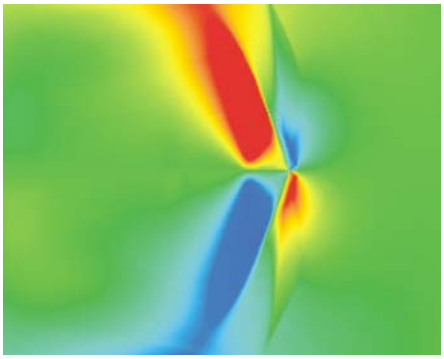

Fig. 9. Intersonic mode I crack. The plot shows a mode I crack in a strongly stiffening material ($k_1 = 4k_0$) propagating faster than the shear wave speed [30].

becomes intersonic, as shown by the Mach cones of shear wave front depicted in Fig. 9.

We have also simulated a shear-dominated mode II crack using the biharmonic stiffening potential. We define $r_{break} = 1.17$, and r_{on} is chosen slightly below r_{break} to keep the hyperelastic region small. The dynamic loading is stopped soon after the daughter crack is nucleated. The result is shown in Figure 10 which plots a sequence of snapshots of a moving mode II supersonic crack. The daughter crack nucleated from the mother crack propagates supersonically through the material, although the hyperelastic zone remains localized to the crack tip region. Supersonic mode II crack propagation has been observed previously by Abraham and co-workers [13] using an anharmonic stiffening potential. However, a clearly defined hyperelastic zone could not be specified in their simulations. Our result proves that a local hyperelastic stiffening effect at the crack tip causes supersonic crack propagation, in clear contrast to the linear continuum theory.

The observation of super-Rayleigh and intersonic mode I cracks, as well as supersonic mode II cracks, clearly contradicts the prediction by the classical linear elastic theories of fracture [14].

3.6 Characteristic energy length scale χ

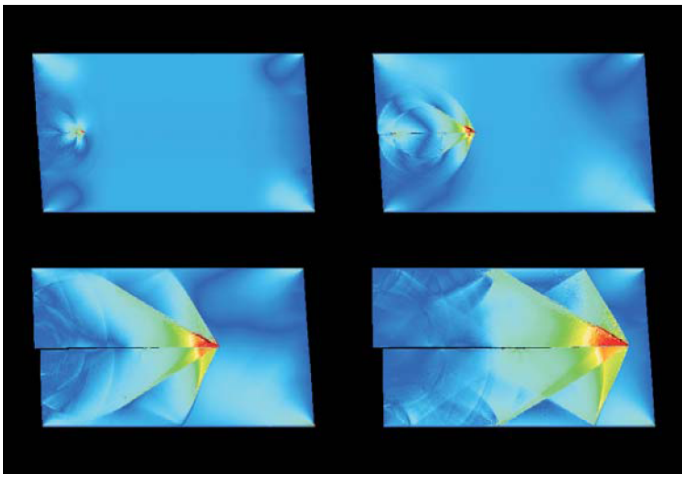

Fig. 10. Sequence of snapshots showing supersonic propagation of a crack under shear loading. A small localized hyperelastic region (not shown here; see reference [30]) at the crack tip leads to crack speeds faster than both shear and longitudinal wave speeds in the material [30].

The problem of a super-Rayleigh mode I crack in an elastically stiffening material is somewhat analogous to Broberg's [73] problem of a mode I crack propagating in a stiff elastic strip embedded in a soft matrix. The geometry of this problem is shown in Fig. 11. Broberg [73] has shown that, when such a crack propagates supersonically with respect to the wave speeds of the surrounding matrix, the energy release rate can be expressed in the form

$$G = \frac{\sigma^2 h}{E} f(v, c_1, c_2) \tag{14}$$

where σ is the applied stress, h is the half width of the stiff layer and f is a non-dimensional function of crack velocity and wave speeds in the strip and the surrounding matrix (c_1, c_2). The dynamic Griffith energy balance requires $G = 2\gamma$, indicating that crack propagation velocity is a function of the ratio h/χ where $\chi \sim \gamma E / \sigma^2$ can be defined as a characteristic length scale for local energy flux. By dimensional analysis, the energy release rate of our hyperelastic stiffening material is expected

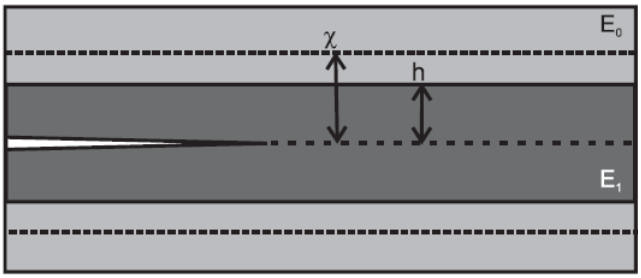

Fig. 11. Geometry of the Broberg problem [30, 73], consisting of a crack embedded in a stiff layer (high wave velocities, Young's modulus E_1) surrounded by soft medium (low wave velocities, Young's modulus E_0).

to have similar features except that Broberg's strip width h should be replaced by a characteristic size of the hyperelastic region r_H. Therefore, we introduce the concept of a characteristic length

$$\chi = \beta \frac{\gamma E}{\sigma^2} \tag{15}$$

for local energy flux near a crack tip. The coefficient β may depend on the ratio between hyperelastic and linear elastic properties. We have simulated the Broberg problem and found that the mode I crack speed reaches the local Rayleigh wave speed as soon as h/χ reaches unity. Numerous simulations verify that the scaling law in eq. (7) holds when γ, E and σ is changed independently. The results are shown in Figure 12. From the simulations, we estimate numerically $\beta \approx 87$ and the characteristic energy length scale $\chi \approx 750$.

The existence of a characteristic length for local energy flux near the crack tip has not been discussed in the literature and plays the central role in understanding the effect of hyperelasticity. Under a particular experimental or simulation condition, the relative importance of hyperelasticity is determined by the ratio r_H / χ. For small r_H / χ, the crack dynamics is dominated by the global linear elastic properties since much of the energy transport necessary to sustain crack motion occurs in the linear elastic region. However, when r_H / χ approaches unity, as is

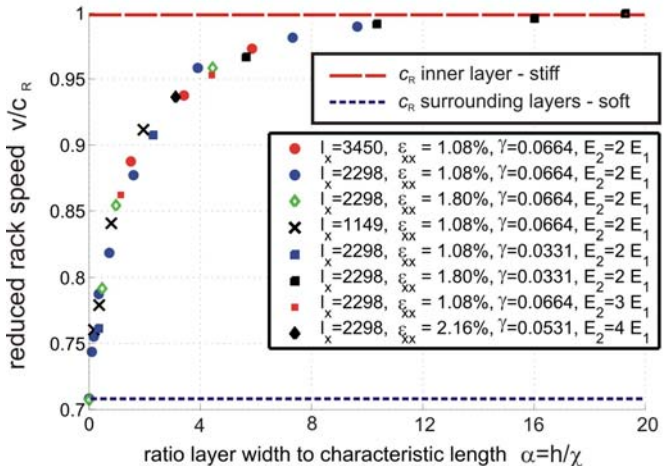

Fig. 12. Calculation results of the geometry defined in the Broberg problem [30]. The plot shows results of different calculations where the applied stress, elastic properties and fracture surface energy are independently varied. In accordance with the concept of the characteristic energy length scale, all points fall onto the same curve and the velocity depends only on the ratio h / χ.

the case in some of our molecular dynamics simulations, the dynamics of the crack is dominated by local elastic properties because the energy transport required for crack motion occurs within the hyperelastic region.

The concept of energy characteristic length χ immediately provides an explanation how the classical barrier for transport of energy over large distances can be undone by rapid transport near the tip.

3.7 Discussion and Conclusions

We have shown that local hyperelasticity has a significant effect on the dynamics of brittle crack speeds and have discovered a characteristic length associated with energy transport near a crack tip. The assumption of linear elasticity fails if there is a hyperelastic zone in the vicinity of the crack tip comparable to the energy characteristic length. Therefore, we conclude that hyperelasticity is crucial for understanding and

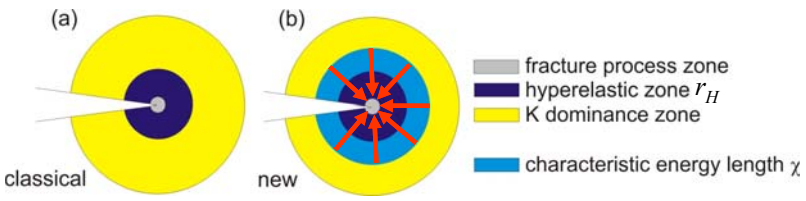

Fig. 13 Different length scales associated with dynamic fracture. Subplot (a) shows the classical picture, and subplot (b) shows the picture with the new concept of the characteristic energy length χ, describing from which region energy flows to a moving crack. The parameter χ is on the order of a few millimeters for 0.1% shear strain in PMMA [30]. Hyperelasticity governs dynamic fracture when the size of the hyperelastic region (r_H) is on the order of the region of energy transport (χ), or $r_H / \chi >> 1$ [30].

predicting the dynamics of brittle fracture. Our simulations prove that even if the hyperelastic zone extends only a small area around the crack tip, there may still be important hyperelastic effects on the limiting speed. If there is a local softening effect, we find that the limiting crack speed is lower than in the case of harmonic solid.

Our study has shown that hyperelasticity dominates the energy transport process when the zone of hyperelastic zone becomes comparable to the characteristic length

$$\chi \sim \frac{\gamma E}{\sigma_0^2}. \tag{16}$$

Under normal experimental conditions, the magnitude of stress may be one or two orders of magnitude smaller than that under MD simulations. In such cases, the characteristic length χ is relatively large and the effect of hyperelasticity on effective velocity of energy transport is relatively small. However, χ decreases with the square of the applied stress. At about one percent of elastic strain as in our simulations, this zone is already on the order of a few hundred atomic spacing and significant hyperelastic effects are observed. The concept of the characteristic length χ is summarized in Figure 13.

Our simulations indicate that the universal function $A(v/c_R)$ in the classical theory of dynamic fracture is no longer valid once the hyperelastic zone size r_H becomes comparable to the energy characteristic length χ. Linear elastic fracture mechanics predicts that the energy release rate of a mode I crack vanishes for all velocities in excess of the Rayleigh wave speed. However, this is only true if $r_H / \chi << 1$. A hyperelastic theory of dynamic fracture should incorporate this ratio into the universal function so that the function should be generalized as $A(v/c_R, r_H / \chi)$. The local hyperelastic zone changes not only the near-tip stress field within the hyperelastic region, but also induces a finite change in the integral of energy flux around the crack tip. A single set of global wave speeds is not capable of capturing all phenomena observed in dynamic fracture.

We believe that the length scale χ, heretofore missing in the existing theories of dynamic fracture, will prove to be helpful in forming a comprehensive picture of crack dynamics. In most engineering and geological applications, typical values of stress are much smaller than those in MD simulations. In such cases, the ratio r_H / χ is small and effective speed of energy transport is close to predictions by linear elastic theory. However, the effect of hyperelasticity will be important for highly stressed materials, such as thin films or nanostructured materials, as well as for materials under high speed impact.

4. Dynamical crack tip instabilities

Cracks moving at low speeds create atomically flat mirror-like surfaces, whereas cracks at higher speeds leave misty and hackly fracture surfaces. This change in fracture surface morphology is a universal phenomenon found in a wide range of different brittle materials. The underlying physical reason of this instability has been debated over an extensive period of time.

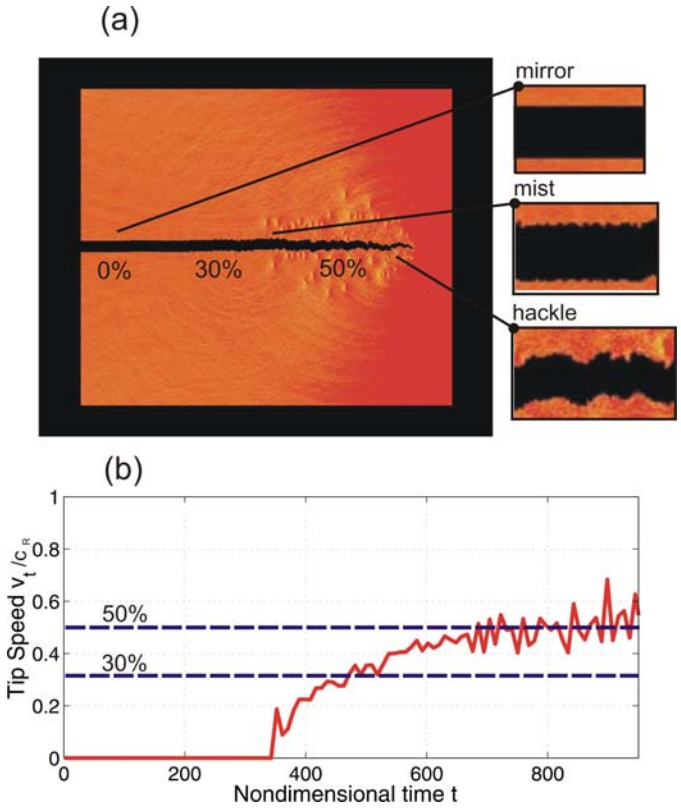

Fig. 14. Crack propagation in a Lennard-Jones (see eq. (2)) system as reported earlier [22, 24]. Subplot (a) shows the σ_{xx}-field and indicates the dynamical mirror-mist-hackle transition as the crack speed increases. The crack velocity history (normalized by the Rayleigh-wave speed) is shown in subplot (b).

Most existing theories of fracture assume a linear elastic stress-strain law. However, from a hyperelastic point of view, the relation of stress and strain in real solids is strongly nonlinear near a moving crack tip. Using massively parallel large-scale atomistic simulations, we show that hyperelasticity also plays an important role in dynamical crack tip instabilities. We find that the dynamical instability of cracks can be regarded as a competition between different instability mechanisms

controlled by local energy flow and local stress field near the crack tip. We hope the simulation results can help explain controversial experimental and computational results.

4.1 Introduction

Here we focus on the instability dynamics of rapidly moving cracks. In several experimental [25, 64, 74, 75] and computational [20, 22, 26, 76, 77] studies, it was established that the crack face morphology changes as the crack speed increases, a phenomenon which has been referred to as the dynamical instability of cracks. Up to a critical speed, newly created crack surfaces are mirror flat (atomistically flat in MD simulations), whereas at higher speeds, the crack surfaces start to roughen (mist regime) and eventually becomes very rough (hackle regime). This is found to be a universal behavior that appears in various brittle materials, including ceramics, glasses and polymers. This dynamical crack instability has also been observed in computer simulation [20, 22, 26, 76, 77]. The result of a large-scale MD simulation illustrating the mirror-mist-hackle transition is shown in Fig. 14.

Despite extensive studies in the past, previous results have led to numerous discrepancies that remain largely unresolved up to date. For example, linear elasticity analyses first carried out by Yoffe [78] predict that the instability speed of cracks is about 73% of the Rayleigh-wave speed [14, 15], as the circumferential hoop stress exhibits a maximum at an inclined cleavage plane for crack speeds beyond this critical crack speed. This is in sharp contrast to observations in several experiments and computer simulations. Experiments have shown that the critical instability speed can be much lower in many materials. In 1992, Fineberg *et al*. [25, 64] observed an instability speed at about one third of the Rayleigh wave speed, which significantly deviates from Yoffe's theory [78]. Similar observations were made in a number of other experimental studies in different classes of materials (e.g. crystalline silicon, polymers such as PMMA). The mirror-mist-hackle transition at about one third of the Rayleigh-wave speed was also observed in the large-scale MD simulations carried out by Abraham *et al.* in 1994 [22]

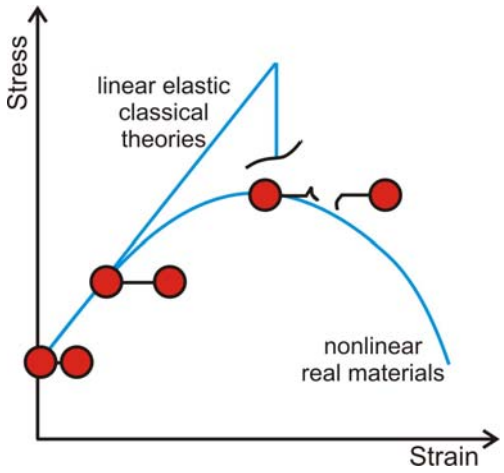

Fig. 15. The concept of hyperelastic softening close to bond breaking, in comparison to the linear elastic, bond-snapping approximation.

(see Fig. 14). The instability issue is further complicated by recent experiments which show stable crack propagation at speeds even beyond the shear wave speed in rubber-like materials [79]. The existing theoretical concepts seem insufficient to explain the various, sometimes conflicting, results and observations made in experimental and numerical studies.

The dynamical crack instability has been a subject of numerous theoretical investigations in the past decades, and several theoretical explanations have been proposed. First, there is Yoffe's model [78] which shows the occurrence of two symmetric peaks of normal stress on inclined cleavage planes at around 73% of the Rayleigh-wave speed. Later, Gao [80] proved that Yoffe's model is consistent with a criterion of crack kinking into the direction of maximum energy release rate. Eshelby [81] and Freund [82] made an argument that the dynamic energy release rate of a rapidly moving crack allows the possibility for the crack to split into multiple branches at a critical speed of about 50% of the Raleigh speed. Marder and Gross [26] presented an analysis which

included the discreteness of atomic lattice [16], and found instability at a speed similar to those indicated by Yoffe's, Eshelby's and Freund's models . Abraham *et al.* [24] have suggested that the onset of instability can be understood from the point of view of reduced local lattice vibration frequencies due to softening at the crack tip [22, 24], and also discussed the onset of the instability in terms of the secant modulus [83].

Heizler *et al*.[84] investigated the onset of crack tip instability based on lattice models using linear stability analysis of the equations of motion including the effect of dissipation. These authors observed a strong dependence of the instability speed as a function of smoothness of the atomic interaction and the strength of the dissipation, and pointed out that Yoffe's picture [78] may not be sufficient to describe the instability. Gao [62, 63] attempted to explain the reduced instability speed based on the concept of hyperelasticity within the framework of nonlinear continuum mechanics. The central argument for reduced instability speed in Gao's model is that the atomic bonding in real materials tends to soften with increasing strain, leading to the onset of instability when the crack speed becomes faster than the local wave speed.

Despite important progresses in the past, there is so far still no clear picture of the mechanisms governing dynamical crack instability. None of the existing models have been able to explain all experimental and numerical simulations with a universal understanding applicable to a wide range of materials.

We hypothesize that hyperelasticity is the key to understanding the existing discrepancies among theory, experiments and simulations on dynamical crack instability. We will show that there exist two primary mechanisms which govern crack instability. The first mechanism is represented by Yoffe's model which shows that the local stress field near the crack tip can influence the direction of crack growth. However, Yoffe's model is not sufficient. The second mechanism is represented by Gao's model [62, 63], which shows that hyperelastic softening drastically reduces the speed of energy transport directly ahead of the crack tip; hyperelasticity induces an anisotropic distribution of local wave speed near the crack tip and causes the crack to kink off its propagation path.

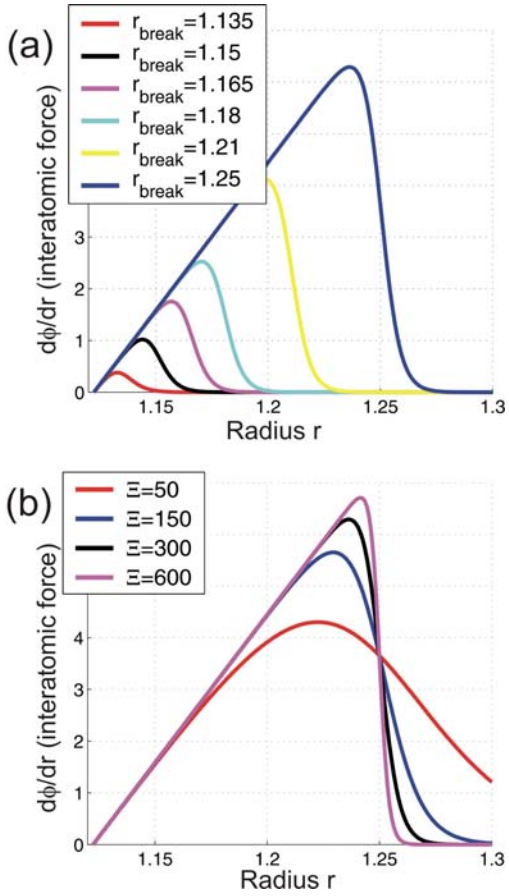

Fig. 16. Force versus atomic separation for various choices of the parameters r_{break} and Ξ. Whereas r_{break} is used to tune the cohesive stress in the material, Ξ is used to control the amount of softening close to bond breaking.

Figure 15 illustrates the concept of hyperelastic softening in contrast to linear elastic behavior. We demonstrate that Yoffe's model and Gao's model are two limiting cases of dynamical crack instability; the former corresponds to completely neglecting hyperelasticity (Yoffe) and the latter corresponds to assuming complete dominance of local hyperelastic zone (Gao). We use large scale MD simulations to show

that the crack tip instability speeds for a wide range of materials behaviors fall between the predictions of these two models.

In the spirit of "model materials" as introduced in Section 3, we develop a new, simple material model which allows a systematic transition from linear elastic to strongly nonlinear material behaviors, with the objective to bridge different existing theories and determine the conditions of their validity. By systematically changing the large-strain elastic properties while keeping the small-strain elastic properties constant, the model allows us to tune the size of hyperelastic zone and to probe the conditions under which the elasticity of large strains governs the instability dynamics of cracks. In the case of linear elastic model with bond snapping, we find that the instability speed agrees well with the predicted value from Yoffe's model. We then gradually tune up the hyperelastic effects and find that the instability speed increasingly agrees with Gao's model. In this way, we achieve, for the first time, a unified treatment of the instability problem leading to a generalized model that bridges Yoffe's linear elastic branching model to Gao's hyperelastic model.

4.2 Atomistic modelling

Although simple pair potentials do not allow drawing conclusions for unique phenomena pertaining to specific materials, they enable us to understand universal, generic relationships between potential shape and fracture dynamics in brittle materials; in the present study we use a simple pair potential that allows the hyperelastic zone size and cohesive stress to be tuned. The potential is composed of a harmonic function in combination with a smooth cut-off of the force based on the Fermi-Dirac (F-D) distribution function to describe smooth bond breaking. We do not include any dissipative terms. The force versus atomic separation is expressed as

$$\frac{d\phi}{dr}(r) = k_0(r - r_0)\left[\exp\left(r\frac{\Xi}{r_{break}} - \Xi\right) + 1\right]^{-1} \tag{17}$$

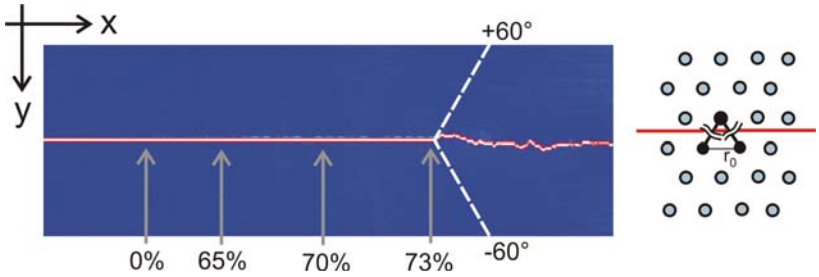

Fig. 17. Crack propagation in a homogeneous harmonic solid. When the crack reaches a velocity of about 73 percent of Rayleigh wave speed, the crack becomes unstable in the forward direction and starts to branch (the dotted line indicates the 60° plane of maximum hoop stress) [60].

Assuming that the spring constant k_0 is fixed, the potential has two additional parameters, r_{break} and Ξ. The parameter r_{break} (corresponding to the Fermi energy in the F-D-function) denotes the critical separation for breaking of the atomic bonds and allows tuning the breaking strain as well as the cohesive stress at bond breaking. In particular, we note that

$$\sigma_{coh} \sim r_{break} . \tag{18}$$

The parameter Ξ (corresponding to the temperature in the F-D-function) describes the amount of smoothing at the breaking point.

In addition to defining the small-strain elastic properties (by changing the parameter k_0), the present model allows us to control the two most critical physical parameters describing hyperelasticity, (i) cohesive stress (by changing the parameter r_{break}), and (ii) the strength of softening close to the crack tip (by changing the parameter Ξ).

Figure 16 depicts force versus atomic separation of the interatomic potential used in our study. The upper part shows the force versus separation curve with respect to changes of r_{break}, and the lower part shows the variation in shape when Ξ is varied. For small values of Ξ (around 50), the softening effect is quite large. For large values of Ξ (beyond 1,000), the amount of softening close to bond breaking becomes very small, and the solid behaves like one with snapping bonds. The parameter r_{break} allows the cohesive stress σ_{coh} to be varied

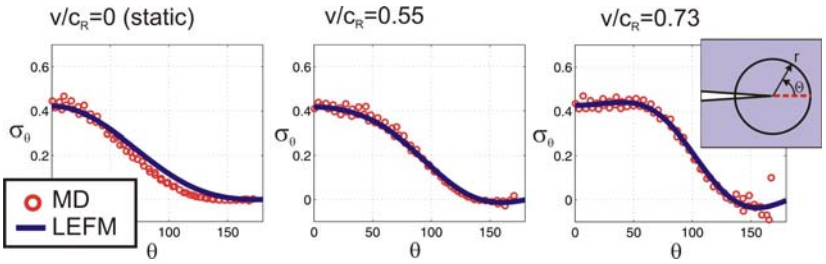

Fig. 18 Comparison between hoop stresses calculated from molecular-dynamics simulation with harmonic potential and those predicted by linear elastic theory [14] for different reduced crack speeds v/c_R [29, 60]. The plot clearly reveals development of a maximum hoop stress at an inclined angle at crack speeds beyond 73% of the Rayleigh-wave speed.

independently. This model potential also describes the limiting cases of material behavior corresponding to Yoffe's model (linear elasticity with snapping bonds) and Gao's model (strongly nonlinear behavior near the crack tip).

Yoffe's model predicts that the instability speed only depends on the small-strain elasticity. Therefore, the instability speed should remain constant at 73% of the Rayleigh-wave speed, irregardless of the choices of the parameters r_{break} and Ξ. On the other hand, Gao's model predicts that the instability speed is *only* dependent on the cohesive stress σ_{coh} (and thus r_{break}):

$$v_{inst}^{Gao} = \sqrt{\frac{\sigma_{coh}}{\rho}} \propto \sqrt{\frac{r_{break}}{\rho}} \tag{19}$$

(note that ρ denotes the density, as defined above). According to Gao's model, variations in the softening parameter Ξ should *not* influence the crack instability speed.

In most of earlier computational studies, the analysis was performed only for a single interatomic potential, such as done for a LJ potential by Abraham *et al*. [22]. It remains unclear how the nature and shape of the atomic interaction affects the instability dynamics. Here we propose systematic numerical studies based on continuously varying potential

parameters r_{break} and Ξ. Our investigations will focus on the predictions of Gao's model versus those of Yoffe's model.

4.3 Atomistic modeling results: Hyperelasticity governs crack tip instabilities

We have performed a series of numerical experiments by systematically varying the potential parameters r_{break} and Ξ. We start with harmonic systems serving as the reference and then increase the strength of the hyperelastic effect to study the dynamics of crack tip instability in hyperelastic materials.

4.3.1 Harmonic potential – the linear elastic reference system

We find that cracks in homogeneous materials with linear elastic properties (harmonic potential, achieved by setting Ξ to infinity) show a critical instability speed of about 73% of the Rayleigh-wave speed, independent of the choice of r_{break}. The crack surface morphology is shown in Fig. 17. This observation is in quantitative agreement with the key predictions of Yoffe's model.

We find that the occurrence of the instability can be correlated with the development of a bimodal hoop stress as proposed by Yoffe, as is shown in the sequence of hoop stress snapshots as a function of increasing crack speed depicted in Fig. 18. We conclude that in agreement with Yoffe's prediction, the change in deformation field governs the instability dynamics in the harmonic systems.

4.3.2 Hyperelastic materials behavior in real materials

It is observed that crack dynamics changes drastically once increasingly stronger softening is introduced at the crack tip and linear elastic Yoffe model fails to describe the instability dynamics.

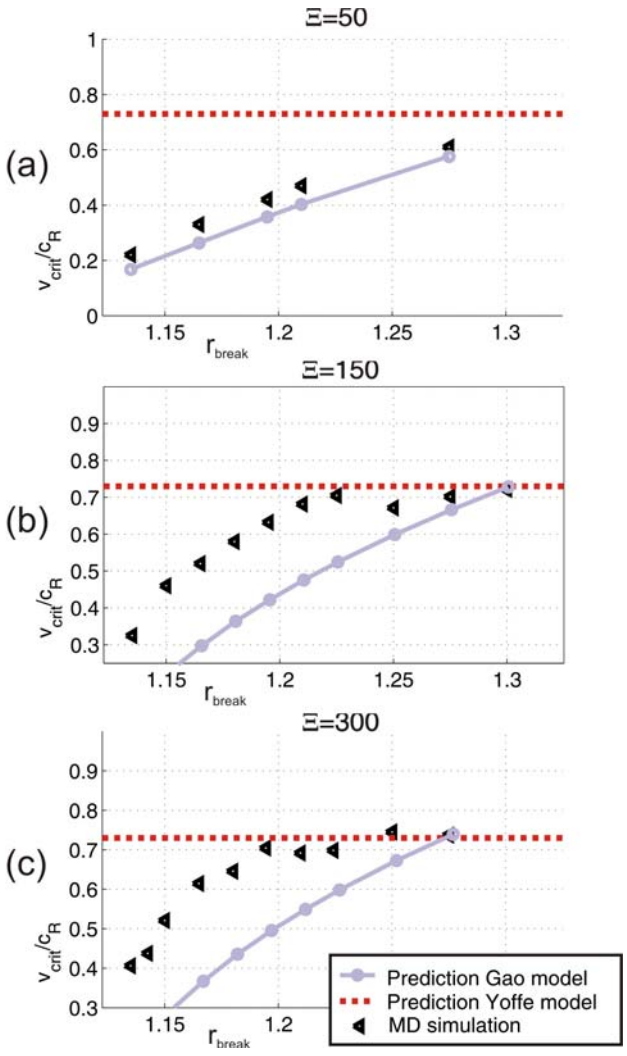

Fig. 19 The critical instability speed as a function of the parameter r_{break}, for different choices of Ξ. The results show that the instability speed varies with r_{break} and thus with the cohesive stress as suggested in Gao's model [62, 63], but the Yoffe speed [78] seems to provide an upper limit for the instability speed. The critical instability speeds are normalized with respect to the local Rayleigh-wave speed, accounting for a slight stiffening effect as shown in Figure 4.

The predictions by Yoffe's model are included in Fig. 19 as the red line, and the predictions by Gao's model are plotted as the blue points. As seen in Fig. 19, we observe that for any choice of r_{break} and Ξ, the instability speed lies in between the prediction by Gao's model and that by Yoffe's model. Whether it is closer to Gao's model or to Yoffe's model depends on the choice of r_{break} and Ξ.

For small values of r_{break} and Ξ, we find that the instability speed depends on the cohesive stress, which is a feature predicted by Gao's model.

Further, the instability speed seems to be limited by the Yoffe speed (as can be confirmed in Fig. 19 for $\Xi = 150$ and $\Xi = 300$ for large values of r_{break}). Whereas the observed limiting speeds increase with r_{break} for $r_{break} < 1.22$, they saturate at the Yoffe speed of 73% of Rayleigh-wave speed for larger values of $r_{break} \geq 1.22$ (see Fig. 19, bottom curve for $\Xi = 300$). In this case, the instability speed is independent of r_{break} and independent of Ξ. This behavior is reminiscent of Yoffe's deformation controlled instability mechanism and suggests a change in governing mechanism for the instability speed: The instability speed becomes governed by a Yoffe-like deformation field mechanism for $r_{break} \geq 1.22$, whereas the instability seems to be influenced by the cohesive-stress for $r_{break} < 1.22$. We find a similar transition for different choices of Ξ ranging from $\Xi = 50$ to $\Xi = 1{,}500$, with different values of r_{break} at which the transition is observed.

These results indicate that the instability speed depends on the strength of softening (parameter Ξ) and on the cohesive stress close to bond breaking (parameter r_{break}).

4.4 The modified instability model

We observe that the first derivative of the instability speed with respect to the cohesive stress in our MD simulations agrees reasonably well with Gao's model. However, the observed instability speed differs from Gao's model by a constant value which seems to depend on the softening parameter Ξ. We measure the deviation from Gao's model by a shift parameter $v_{shift} = v_{inst}^{MD} - v_{inst}^{Gao}$ which is a function of Ξ. The curve is shown in Figure 20.

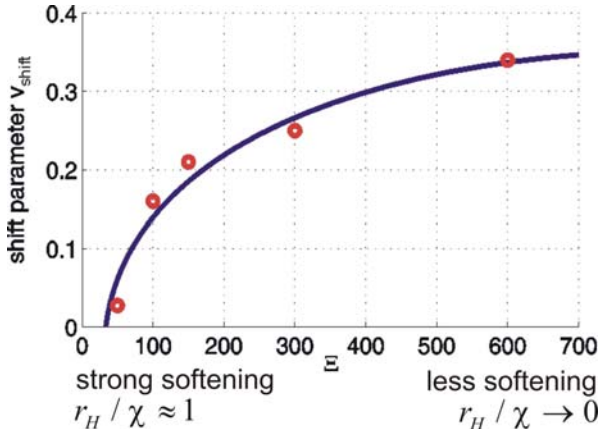

Fig. 20 Change of shift parameter v_{shift} as a function of the smoothing parameter Ξ. Small values of Ξ lead to cases where hyperelasticity dominates the instability onset ($r_H / \chi \approx 1$), and larger values of Ξ correspond to the case when the importance of hyperelasticity vanishes and the instability onset is governed by changes in the deformation field ($r_H / \chi \to 0$)

The physical interpretation of v_{shift} is that it accounts for the relative importance of hyperelastic softening close to the crack tip: Gao's model corresponds to the *limiting case* when the softening region is large and completely dominates the energy flow, and it therefore constitutes the *lower limit* for the instability speed. Indeed, we find that for very strong softening, that is, when $\Xi \to 0$, v_{shift} vanishes (Figure 20). In contrast, v_{shift} assumes larger values in the case of vanishing softening as $\Xi \to \infty$. The physical significance of this parameter can be understood from the perspective of the characteristic energy length scale of dynamic fracture

$$\chi \sim \frac{\gamma E}{\sigma^2} \tag{20}$$

proposed earlier (see Section 3) [30]. The characteristic energy length scale χ describes the region from which energy flows to the crack tip to drive its motion. If the size of the softening region is comparable to χ, *i.e.*,

$$\frac{r_H}{\chi} >> 1, \tag{21}$$

hyperelasticity dominates energy flow, thus $v_{shift} \to 0$, and the predictions of Gao's model should be valid. In contrast, if the size of the softening region is smaller than χ, *i.e.*

$$\frac{r_H}{\chi} \approx 0, \tag{22}$$

hyperelasticity plays a reduced role in the instability dynamics and the purely hyperelastic model becomes increasingly approximate, so that v_{shift} takes larger values and eventually Yoffe's model of deformation field induced crack kinking begins to play a governing role. The shift parameter $v_{shift}(\Xi)$ should therefore depend on the relative size of the hyperelastic region compared to the characteristic energy flow

$$v_{shift} = f\left(\frac{r_H}{\chi}\right). \tag{23}$$

With the new parameter v_{shift}, the instability speed can be expressed as

$$v_{inst} = v_{shift}\left(\frac{r_H}{\chi}\right) + \sqrt{\frac{\sigma_{coh}}{\rho}} \tag{24}$$

Based on the results of our numerical experiments, we propose that eq. (19) and the Yoffe model should be combined to predict the onset of instability at a critical speed. The critical crack tip instability speed is then given by

$$v_{inst}^{\text{mod}} = \min\left(v_{YOFFE}, v_{shift}\left(\frac{r_H}{\chi}\right) + \sqrt{\frac{\sigma_{coh}}{\rho}}\right) \tag{25}$$

where $v_{YOFFE} \approx 0.73 c_R$ is a constant, independent on the hyperelastic properties. We refer to this model as the modified instability model. Fig. 21 compares the predictions by eq. (25) with the MD simulation results (dashed curve).

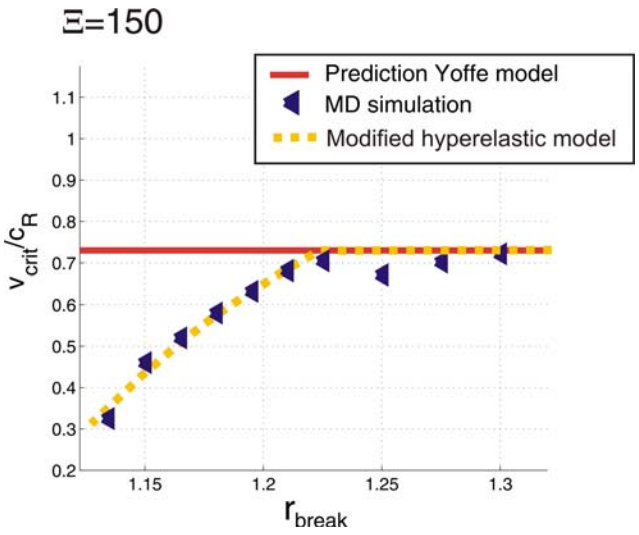

Fig. 21. Comparison of the *modified instability model* (see eq. (25)) for $\Xi = 150$ with the MD simulation results, showing the transition from an energy flow controlled instability mechanism to a deformation field controlled mechanism.

4.5 Stiffening materials behavior: Stable intersonic mode I crack propagation

A generic behavior of many rubber-like polymeric materials is that they stiffen with strain. What happens to crack instability dynamics in such materials? Recent experiments [79] have shown intersonic mode I crack propagation in rubber-like materials with elastic stiffening behaviors. According to the existing theories, such high speed crack propagation should not be possible in homogeneous materials. We hypothesize that local stiffening near the crack tip may lead to a locally enhanced Yoffe speed and enhanced energy flow, so that the onset of crack tip instability is shifted to higher velocities.

Our simulations are based on a simple model in which we change the large-strain spring constant and small-strain spring constant, similar to studies described in the previous section except for the smoothing part

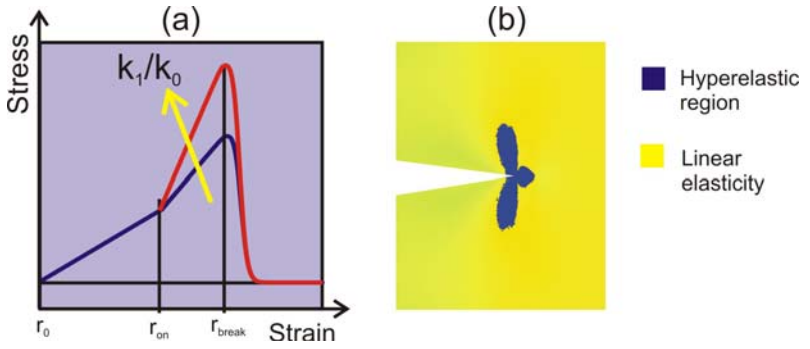

Fig. 22. Subplot (a): Schematic of stiffening materials behaviour as assumed in Section 4.5. Subplot b): Extension of the hyperelastic stiffening region for the case of $r_{break} = 1.17$, $r_{on} = 1.1375$ and $k_1 / k_0 = 4$. Despite the fact that the stiffening hyperelastic region is highly localized to the crack tip and extends only a few atomic spacings, the crack instability speed is larger than the Rayleigh-wave speed.

near bond snapping. The model is depicted schematically in Fig. 22(a). Upon a critical atomic separation r_{on} (we choose $r_{on} = 1.1375$), the spring constant of the harmonic potential is changed and switched to a new "local" large-strain value.

Knowledge of r_{on} allows for clear definition of the extension of the hyperelastic zone near the crack tip (for details see reference [30]), as can be verified in Fig. 8 and Fig. 22(b). As described earlier, here we also use the F-D-function to smoothly cut off the potential at r_{break}. We discuss two different choices of the ratio $k_1 / k_0 = 2$ and $k_1 / k_0 = 4$.

We observe that if there exists a hyperelastic stiffening zone, the Yoffe speed is *no longer* a barrier for the instability speed and stable crack motion beyond the Yoffe speed can be observed. This behavior is shown in Figure 23. We find that the stronger the stiffening effect, the more rapid the increase of instability speed with increasing value of r_{break} (see the curves for $k_1 / k_0 = 2$ and $k_1 / k_0 = 4$ in Figure 23).

Note that all points fall together once r_{break} becomes comparable to r_{on}, corresponding to the case when no hyperelastic zone is present and the potential is harmonic with smooth F-D bond breaking (here the potential shape is identical because bonds rupture before onset of the

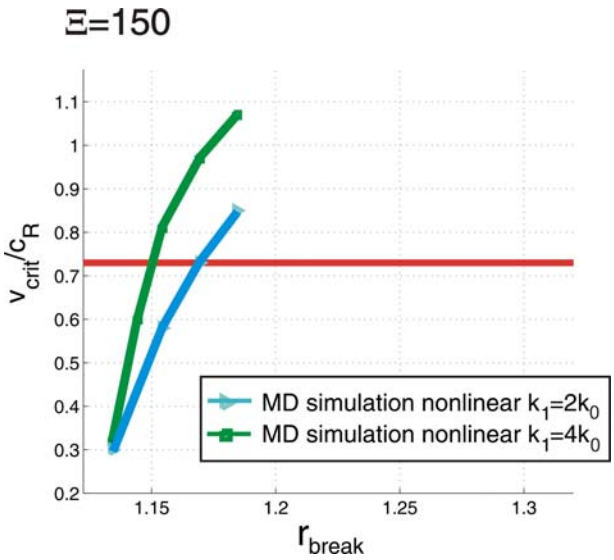

Fig. 23. MD simulation results of instability speed for stiffening materials behaviour, showing stable super-Rayleigh crack motion as observed in recent experiment (see the legends in the lower left). Such observation is in contrast to any existing theories, but can be explained based on the hyperelastic viewpoint.

hyperelastic effect). As can be clearly seen in Fig. 23 for $k_1 / k_0 = 4$, the instability speed can even be super-Rayleigh and approach intersonic speeds.

This is inconsistent with the classical theories but can be understood from a hyperelasticity point of view. This observation suggests that the stiffening materials behavior tends to have a stabilizing effect on straight crack motion.

4.6 Discussion and conclusions

Our simulation studies strongly suggest that the large-deformation elastic properties play a critical role in the instability dynamics of cracks.

Our results indicate that the onset of instability can be understood as a competition between energy flow governed instability (Gao's model

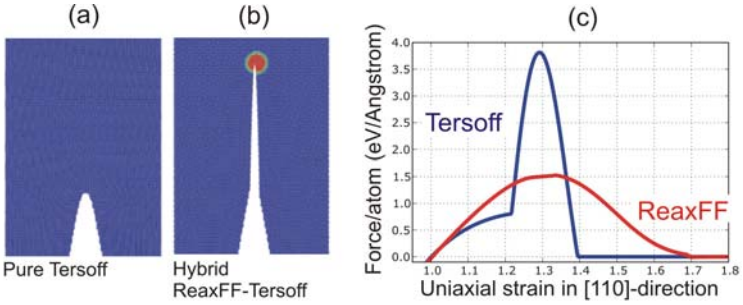

Fig. 24. Importance of accurate large-strain properties of bond breaking during fracture in silicon [85-87]. The results suggest that the large-strain properties close to bond breaking is critical in determining how and under which conditions cracks propagate. Subplot (a) shows results without correct large-strain elasticity, whereas subplot (b) depicts the results with correct large-strain elasticity at bond breaking. The difference of bond breaking is shown in subplot (c), indicating the incorrect behavior of the Tersoff potential at bond breaking.

[62, 63]) and stress field governed instability (Yoffe's model [78]), as summarized in eq. (12). To the best of our knowledge, Eq. (25) describes for the first time this transition between Yoffe's and Gao's model of instability dynamics (see Fig. 21). We hypothesize that the transition between the two mechanisms depends on the relative importance of hyperelasticity around the crack tip, as described by the ratio of the size of the hyperelastic region and the characteristic energy length scale r_H / χ. In most experiments and computers simulations, materials show a strong softening effect. Therefore, hyperelastic softening near the crack tip may explain the reduced instability speed observed in experiments.

In the case of a locally stiffening hyperelastic region, we find that the critical speeds for crack instability could be higher since the *local hyperelastic zone* with local higher wave speed allows for faster energy transport and higher local wave speeds; in this case, the small-strain Yoffe speed is no longer a barrier due to local stiffening. This concept provides a feasible explanation of recent experimental observations of stable mode I cracking at crack velocities beyond the shear wave speed

in homogeneous materials that show a strong stiffening hyperelastic effect (see Fig. 23).

The notion that large-strain elastic properties close to bond breaking are important has recently also been demonstrated in studies of fracture in silicon [86]. Figure 24 shows a comparison of fracture dynamics by changing the description of bond breaking from an empirical Tersoff-type [88] to a first principles description using reactive potentials [89]. Only if a correct quantum mechanical derived description of bond breaking is used, the MD model is capable to reproduce important experimental features of fracture of silicon.

The work reported here, together with the results on the maximum crack speed (see Section 3), strongly suggest that hyperelasticity can play governing roles in dynamic fracture.

5. Dynamic crack propagation along interfaces between dissimilar materials: Mother-, daughter- and granddaughter cracks

Cracking along interfaces has received significant attention in the past decades, both due to technological relevance for example in composite materials, as well as because of scientific interest. In this section, we review recent progress in large-scale atomistic studies of crack propagation along interfaces of dissimilar materials [37, 66, 90].

We consider two linear-elastic material blocks bound together with a weak potential whose bonds snap early upon a critical atomic separation, as shown schematically in Fig. 25. This approach confines crack motion along the interface. In the two blocks, atoms interact with harmonic potentials with different spring constants adjacent to the interface. An initial crack is introduced along the interface and subjected to tensile (section 5.2) and shear (section 5.3) dominated displacement loading along the upper and lower boundaries of the sample.

Under tensile loading, we observe that upon initiation at a critical load, the crack quickly approaches a velocity a few percent larger than the Rayleigh-wave speed of the soft material. After a critical time, a secondary crack is nucleated a few atomic spacings ahead of the crack. This secondary crack propagates at the Rayleigh-wave speed of the stiff material. If the elastic mismatch is sufficiently large (e.g. ten as in our

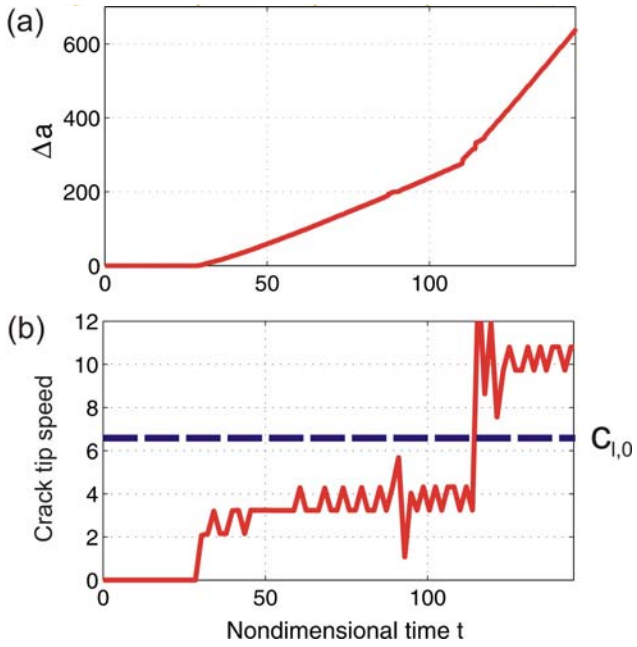

Fig. 26. Crack tip history and crack velocity history for a mode I crack propagating at an interface with X =10 . Subplot (a) shows the crack tip history, and subplot (b) shows the crack tip velocity over time. A secondary daughter crack is born propagating at a supersonic speed with respect to the soft material layer.

study), the secondary crack can be faster than the longitudinal wave speed of the soft material, thus propagating supersonically. At this stage, supersonic crack motion is clearly identified by two Mach cones in the soft material. Our study suggests that such mother-daughter transition mechanism, which has been previously reported for mode II crack motion in homogeneous materials [13, 31, 38], may also play an important role in the dynamics of interfacial cracks under tensile loading. We also include some studies of unconstrained crack motion along interfaces of dissimilar materials, and demonstrate that the crack tends to branch off into the softer region, in agreement with previous study by Xu and Needleman [91, 92].

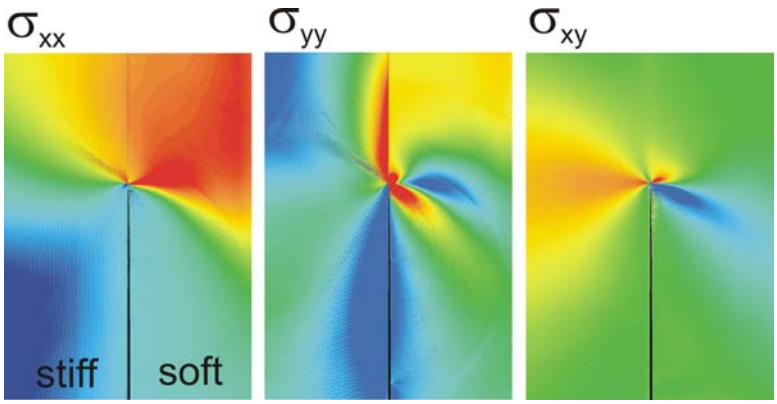

Fig. 27. Stress fields σ_{xx} , σ_{yy} and σ_{xy} for a crack at an interface with elastic mismatch Ξ =10 before the secondary crack is nucleated. The red color corresponds to large stresses, and the blue color to small stresses.

Under shear dominated loading, upon initiation of the crack, we observe that the crack quickly approaches a velocity close to the Rayleigh-wave speed of the soft material. After cruising at this speed for some time, a secondary crack is nucleated at a few atomic spacings ahead of the crack. This secondary crack, also referred to as the daughter crack [37, 38, 93], propagates at the longitudinal-wave speed of the soft material. Shortly after that, a tertiary crack, referred to as the granddaughter crack, is nucleated and begins to move at the longitudinal wave speed of the stiff material. The granddaughter crack is supersonic with respect to the soft material and is clearly identifiable by two Mach cones in the soft material [37]. Our results indicate that the limiting speed of shear dominated cracks along a bi-material interface is the longitudinal wave speed of the stiff material, and that there are two intermediate limiting speeds (Rayleigh and longitudinal wave speeds of the soft material) which can be overcome by the mother-daughter-granddaughter mechanism.

5.1 Atomistic modeling of cracking along a bimaterial interface

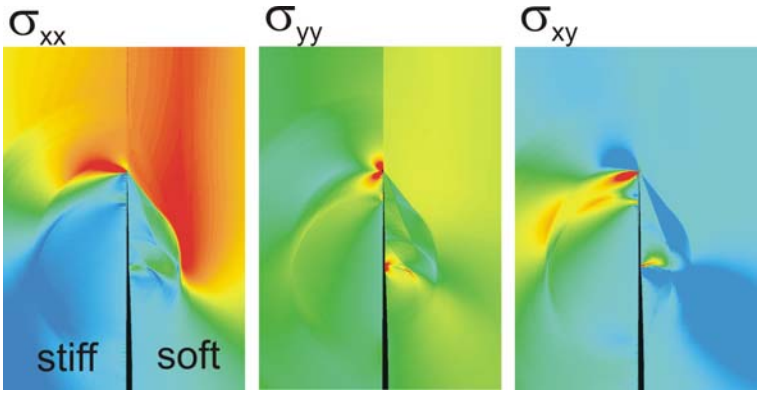

Fig. 28. Stress fields σ_{xx}, σ_{yy} and σ_{xy} for a crack at an interface with elastic mismatch Ξ =10 after the secondary crack is nucleated. In all stress fields, the two Mach cones in the soft material are seen. The red color corresponds to large stresses, and the blue color to small stresses.

To model a crack along an interface between two elastically dissimilar materials, we study two crystal blocks described by harmonic interatomic potentials with different spring constants $k_1 > k_0$. For simplicity, we consider two-dimensional triangular lattices with isotropic elastic properties. The harmonic potential is defined as in eq. (1).

We choose $k_0 = 36/\sqrt[3]{3} \approx 28.57$ with the corresponding Rayleigh-wave speed $c_R \approx 3.4$, shear wave speed $c_s \approx 3.68$ and longitudinal wave speed $c_l \approx 6.36$. The difference in Young's modulus of the two materials can be related to the ratio

$$\Xi = \frac{k_1}{k_0}. \tag{26}$$

The wave speeds c_I (with $I = (R, s, l)$) of the two materials thus differ by a factor $\sqrt{\Xi}$:

$$c_{I,1} = \sqrt{\Xi} \cdot c_{I,0} \tag{27}$$

Atomic bonds across the weak interface have spring constant k_0 and break upon a critical separation $r_{break} = 1.17$.

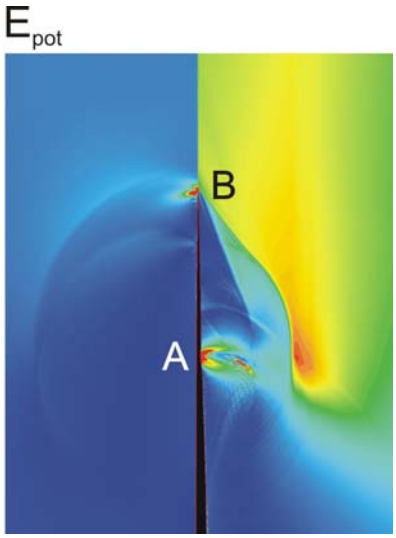

Fig. 29. The potential energy field for a crack at a biomaterial interface with elastic mismatch Ξ =10. Two Mach cones in the soft solid can clearly be observed. The mother (A) and daughter crack (B) are marked in the figure. The mother crack is represented by a surface wave in the soft material after nucleation of the secondary crack.

The simulation slab is subjected to an applied tensile and/or shear strain rate along the upper and lower boundaries, as shown in Fig. 25. The system size is given by $l_x \approx 2{,}298$ and $l_x \approx 4{,}398$. Further details on modeling fracture based on harmonic potentials, as well as a detailed analysis on the elastic and fracture properties can be found elsewhere [13, 30, 31, 38] (see also discussion in previous sections). In homogeneous materials, it has been shown that the simulated results of limiting crack speeds, the energy flow fields and the stress fields near rapidly propagating cracks are in good agreement with continuum mechanics predictions (see results discussed in Section 3).

The geometry of our atomistic model, the loading as well as the crystal orientation of crack propagation is described in Fig. 25. The upper (left) block of the simulation slab is relatively stiff with higher Young's modulus and higher wave speeds than the lower (right) block.

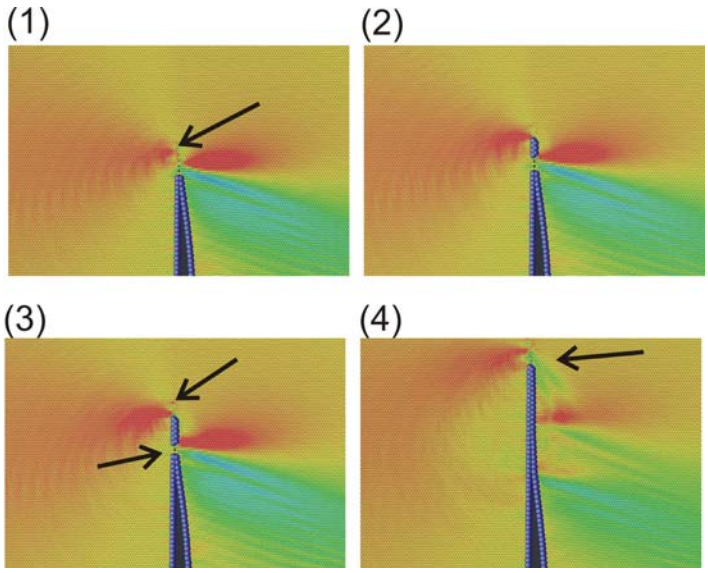

Fig. 30. Atomic details of nucleation of the secondary crack under tensile dominated loading. The plot shows the shear stress field σ_{xy} near the crack tip. Atoms with the energy of a free surface are drawn as larger, bluish atoms. The plot suggests that a maximum peak of the shear stress ahead of the crack tip leads to breaking of atomic bonds and creation of new crack surfaces. After the secondary crack is nucleated, it coalesces with the mother crack and moves supersonically through the material.

5.2 Tensile dominated cracks at bimaterial interfaces: Mother-daughter mechanisms and supersonic fracture

In all cases studied in this paper, the cracked bi-crystal is loaded under tensile loading with a strain rate $\dot{\varepsilon}_{xx} = 0.000{,}1$ (the orientation of the loading is shown schematically in Figure 25) [37, 90]. In some cases, the loading is stopped as indicated in each case. Although there is usually no pure mode I interfacial cracks due to complex stress intensity factors, the stress field near the crack tip is expected to be mode I dominated under pure tensile loading.

5.2.1 Mode I dominated interfacial cracks: Constrained simulations

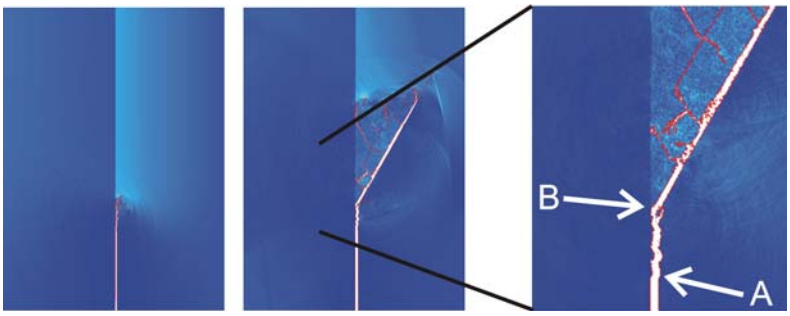

Fig. 31. Crack dynamics in homogeneous material without a weak layer (case (ii)). Unlike in the other cases, in this simulation we allow atomic bonds to break anywhere in the system. We observe that before the daughter crack is nucleated, the crack starts to wiggle and is thus limited in speed. Further, we observe that the crack branches off into the soft material and continues to propagate there. The plot on the right hand side shows a zoom into the crack tip region, showing the initial crack surface roughness (A) and the dominant branch (B) into the soft material. We observe a tendency of branching into the soft region from the wiggling stages (point A, for instance).

All studies reported in this Section are carried out with an elastic mismatch of $\Xi = 10$. Figure 26(a) shows the crack tip history, and Figure 26(b) shows the crack tip velocity over time. The crack nucleates at time $t \approx 35$, and quickly approaches the Rayleigh wave speed of the soft material $v \to c_{r,0} \approx 3.4$. As the loading is increased, the crack speed increases slightly and becomes super-Rayleigh with respect to the soft material. We observe a large, discontinuous jump in the crack velocity at $t \approx 110$, when a secondary crack is nucleated that quickly approaches the Rayleigh speed of the stiff material $v \to c_{r,1} \approx 10.8 > c_{l,0} \approx 6.36$.

The secondary crack is nucleated approximately at a distance $\Delta a \approx 11$ ahead of the mother crack and rapidly propagates at Mach 1.7 with respect to the soft material. Nucleation of the secondary crack under tensile loading is only found under high strain rate loading (here we use $\dot{\varepsilon}_{xx} = 0.000{,}1$). If the strain rate is too low, the crack moves at a sub-Rayleigh speed (soft material) until the solid has separated, without nucleation of secondary cracking. The mechanism of nucleation of a secondary crack is reminiscent of the mother-daughter mechanism predicted by the Burridge-Andrew mechanism [94, 95] and observed in

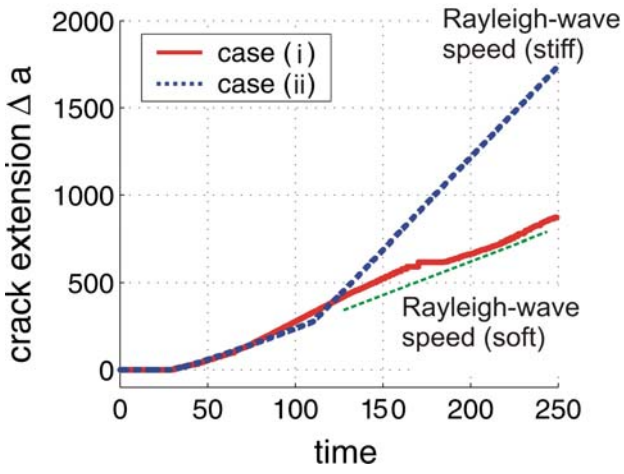

Fig. 32. Crack tip extension history as a function of time for the cases (i) and (ii) described in Section 4. The plot illustrates that once the daughter crack has been nucleated it does not branch off into either the weak or the soft material, but instead continues to propagate along the weak interface. If crack motion is unconstrained from the very beginning, it starts to branch off at low speeds (see also Figure 31) and eventually branches off into the soft material. In this case, a daughter crack is never nucleated.

MD simulations for intersonic mode II cracks in homogeneous solids [13, 31, 38].

These results suggest that a mode I dominated interface crack under very large loading can propagate at the Rayleigh wave speed of the stiffer material, which can exceed the longitudinal wave speed in the soft material. This observation has not been reported in experiments so far, nor has it been predicted by theory. In experimental studies of mode I dominated cracks along bi-material interfaces, the crack speed has been reported to exceed the Rayleigh wave speed of the soft material, but has never been observed to attain supersonic velocities with respect to the soft material.

As the next step, we take a closer look at the deformation fields before and after nucleation of the secondary crack, taking advantage of the "computational microscope" that MD provides. Figure 27 shows the stress field before the secondary crack is nucleated. At the time the

snapshots are taken, the crack propagates at a (slightly) super-Rayleigh speed with respect to the soft material. Since the crack motion is still subsonic, no shock front is observed. Figure 28 shows the stress field and the particle velocity field after nucleation of the secondary crack. The secondary crack propagates supersonically with respect to the soft material and the Mach cones in the right half space (soft material) are clearly visible. Figure 29 shows the potential energy field for a crack after the secondary, supersonic crack is nucleated. The two mach cones can clearly be seen. Similar mother-daughter mechanism for mode I dominated interfacial fracture has also been observed for smaller elastic mismatch ratios $\Xi = 2$, $\Xi = 5$, and $\Xi = 7$ (however, not in all cases crack motion is supersonic with respect to the soft material since the Rayleigh-wave speed of the stiff material may be smaller than the longitudinal wave speed of the soft material).

What is governing nucleation of the secondary crack? MD simulations can be particularly helpful in investigating the atomistic details of the mechanism of nucleation of secondary cracks. In Figure 30, we plot the shear stress field σ_{xy} for several instants in time during nucleation of the secondary crack (note we chose quite small time intervals between the snapshots). Atoms with the energy of a free surface are colored blue and highlighted by larger spheres. The plot suggests that a peak of shear stress ahead of the crack tip may have caused breaking of atomic bonds. After the secondary crack is nucleated, it coalesces with the mother crack and moves supersonically with respect to the soft material. This mechanism via a peak in shear stress is quite similar to the understanding of nucleation of secondary cracks in shear loaded cracks in homogeneous systems as discussed in [38]. We note that the location of the maximum tensile stress σ_{xx} does not coincide with the location of nucleation of the secondary crack; rather, the latter was found to correlate with a peak in shear stress ahead of the mother crack. We there conclude that there exists a peak in shear stress ahead of a mode I dominated interfacial crack moving at the Rayleigh wave speed of the soft material and this peak shear stress leads to subsequent nucleation of a secondary crack which breaks the sound barrier at the soft Raleigh speed.

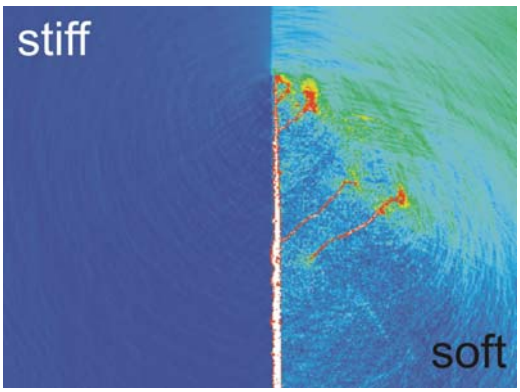

Fig. 33. Crack dynamics at a bimaterial interface with homogeneous fracture energy everywhere in the slab (case (iii)). In this study, the fracture surface energy in both the stiff and soft materials is equal. We observe that the crack continuously branches off into the soft solid and creates numerous small cracks. This indicates a general tendency of the crack to branch off into the soft material.

5.2.2 Unconstrained simulations

In this section, we relieve the constraint that crack propagation be restricted to the interface between the stiff and the soft material (glue). We report the results of three cases: (i) Crack motion is constrained along the interface until the secondary daughter crack is nucleated, and from then on crack motion is left unconstrained (we relieve the constraint at $t = 126$). (ii) Crack motion is unconstrained from the beginning of the simulation; the condition for breaking is given by $r_{\text{break}} = 1.17$ in both stiff and soft solid (therefore, the fracture surface energy is lower in the right half space than in the left half space). (iii) Crack motion is unconstrained from the beginning of the simulation; in contrast to case (ii), here we adjust r_{break} in the left material such that the fracture surface energy is equal to that in the right material so that the slab has a homogeneous fracture energy:

$$r_{break}^{left} = r_0 - \frac{1}{\sqrt{\Xi}}(r_0 - r_{break}^{right}) \tag{28}$$

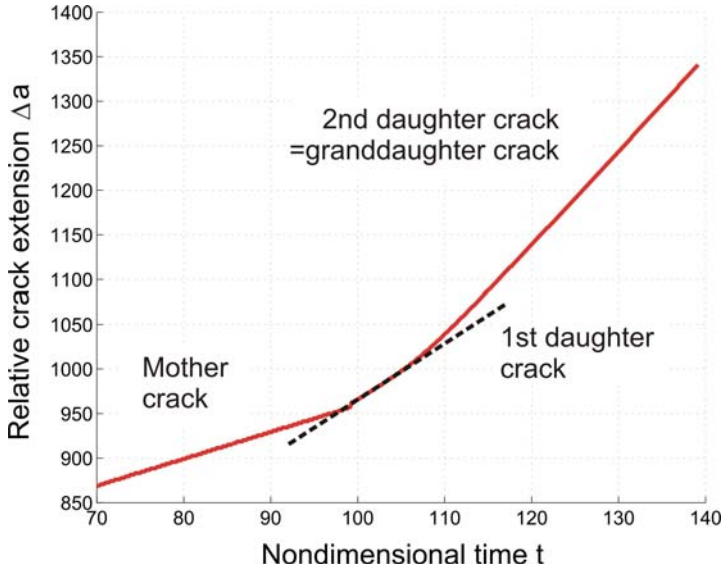

Fig. 34. Crack tip history for a shear loaded crack propagating along an interface with stiffness ratio $\Xi = 3$. This crack tip history plot reveals a mother-daughter-granddaughter mechanism: After a critical time, a secondary crack (the daughter crack) is nucleated ahead of the mother crack. Shortly afterwards, a tertiary crack (the granddaughter crack) is nucleated. The transition in crack speed is from the daughter to the granddaughter is more continuous compared to that from the mother to the daughter (see also the velocity history plot depicted in Fig. 35).

and thus for $r_{break}^{right} = 1.17$ we assume that $r_{break}^{left} = 1.13749$.

In case (i), we observe that the crack continues to move along its original direction and does not branch off into the soft or the stiff material until the bi-crystal is completely broken.

In case (ii), we observe that before the daughter crack is nucleated, the crack starts to wiggle and is thus limited in speed. Figure 29 shows the simulation snapshots of case (ii). We find that the crack branches off into the soft material and continues to propagate there. The plot on the right hand side in Figure 31 shows a zoom into the crack tip region, showing the initial crack surface roughness (A) and the large dominant branch (B) into the soft material.

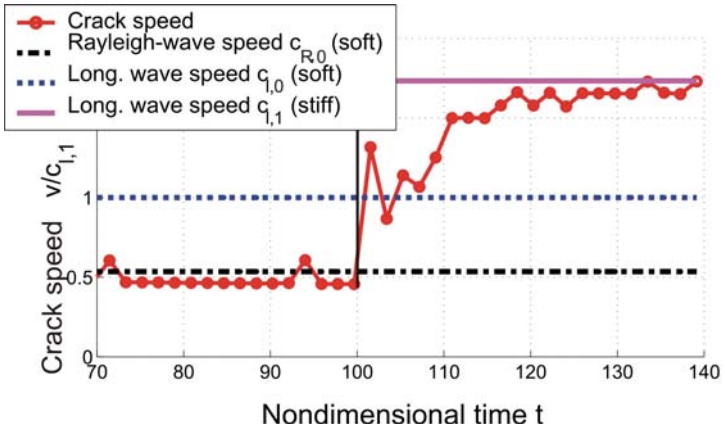

Fig. 35. Crack tip velocity history during the mother-daughter-granddaughter mechanism for a shear loaded crack propagating along an interface with stiffness ratio $\Xi = 3$. The plot is obtained by numerical differentiation of the crack tip history shown in Fig. 2. The crack speed changes abruptly at the nucleation of the daughter crack, and rather continuously as the granddaughter crack is nucleated.

Figure 32 plots the crack tip history for case (i) and case (ii). It clearly reveals that in case (ii) nucleation of a secondary daughter crack does not occur. However, the crack speed increases to speeds beyond the Rayleigh-wave speed of the soft material. In case (i), crack speed remains at the longitudinal wave speed of the stiff material, even after the constraint is relieved.

In case (iii), when the fracture surface energy is equal in the stiff and the soft materials, we observe a tendency of the crack to branch off into the soft region. Figure 33 shows a snapshot at late stages of simulation (here the loading rate was $\dot{\varepsilon}_{xx} = 0.000{,}02$, and loading never stopped). The branching into the soft region (right half) can clearly be recognized.

5.3 Shear dominated cracks at bimaterial interfaces: Observations in MD simulation

While noting that the basic observations here will hold for a range of elastic mismatch ratios, we mainly discuss the results at $\Xi = 3$. The

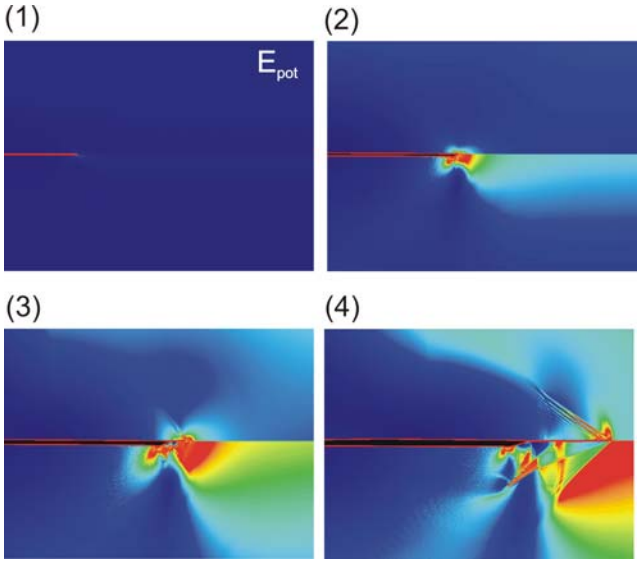

Fig. 36. The plot shows the potential energy field near a shear loaded interface crack with stiffness ratio $\Xi = 3$ (color code: red corresponds to high potential energy and blue corresponds to the potential energy of atoms in a perfect lattice). The plot shows a small section around the crack tip. The crack surfaces are highlighted red. In the upper left plot, the initial configuration with the starting crack is shown. As the loading is increased, the mother crack starts to propagate, eventually leading to secondary and tertiary cracks. Two Mach cones in the soft solid and one Mach cone in the stiff solid can be observed in the lower right figure, suggesting supersonic crack motion with respect to the soft material and intersonic motion with respect to the stiff material.

primary crack is observed to initiate at time $t \approx 34$ and quickly approaches the Rayleigh speed of the soft material $v \to c_{R,0} \approx 3.4$.

Figure 34 shows the history of crack tip location, and Figure 35 that of the crack tip velocity [90]. Both curves are shown over a time interval close to the nucleation of secondary and tertiary cracks. We observe a discontinuous jump in the crack velocity at $t \approx 100$, as the daughter crack is nucleated in front of the mother crack. The daughter crack forms at a distance $\Delta a \approx 10$ ahead of the mother crack and quickly approaches the longitudinal wave speed of the soft material $v \to c_{l,0} \approx 6.36$. The mechanism of nucleation of the daughter crack is

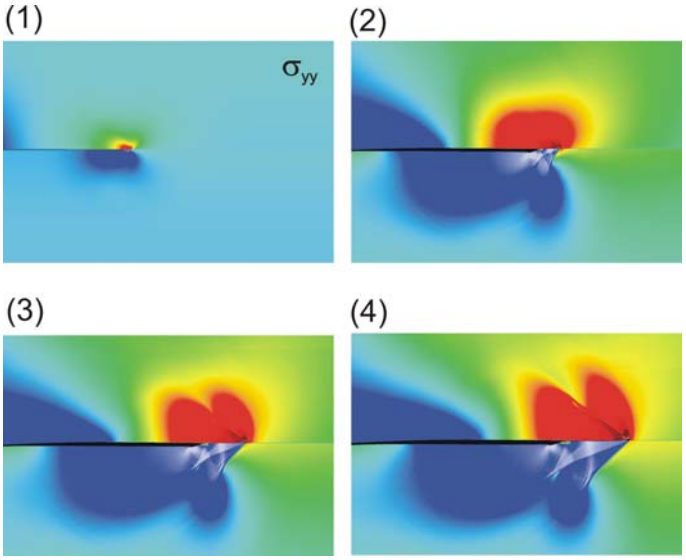

Fig. 37. The plot shows the σ_{vv} stress field near a shear loaded interface crack with stiffness ratio $\Xi = 3$ (color code: red corresponds to high stresses), for a similar sequence as shown in Figure 36. The Mach cones can clearly be seen in snapshot (4).

reminiscent of the mother-daughter mechanism of mode II cracks in homogeneous materials [31, 38].

Shortly after the daughter crack is nucleated, another change in propagation speed is observed at time $t \approx 108$ (see Figures 34 and 35). This is due to initiation of a tertiary granddaughter crack ahead of the daughter crack. The nucleation of the granddaughter crack occurs at a short time ($\Delta t \approx 8$) after nucleation of the daughter crack (Figs. 34 and 35).

The transitions from mother to daughter and daughter to granddaughter cracks are quite sharp, and the crack motion stabilizes after the granddaughter crack is nucleated. Figure 36 shows a few snapshots of the potential energy field from the initial configuration until the birth of the granddaughter crack. A similar sequence is shown in Figure 37, depicting the σ_{yy} stress field.

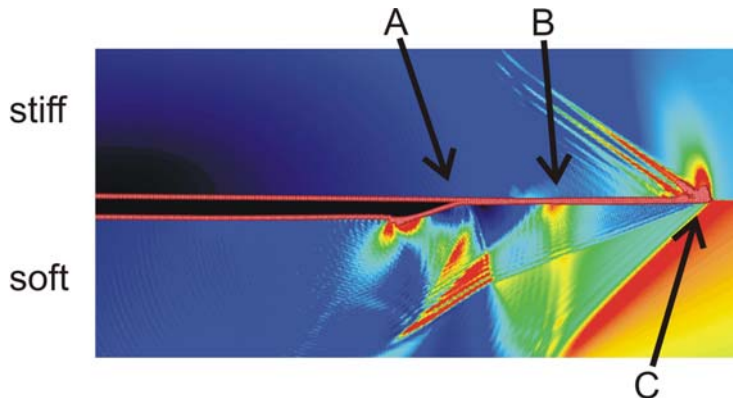

Fig. 38. The plot shows the potential energy field in the vicinity of the crack tip, shortly after nucleation of the granddaughter crack (color code: red corresponds to high potential energy and blue corresponds to the potential energy of atoms in a perfect lattice). The mother, daughter and granddaughter cracks can be identified. In the blow-up on the right, the mother (A), daughter (B), and granddaughter (C) are marked. The mother and daughter cracks are represented by waves of stress concentration in the soft material. For the daughter crack (B), the Mach cone associated with the shear wave speed in the soft material can clearly be observed. The granddaughter crack (C) carries two Mach cones in the soft material.

In Figure 38, we show a blowup plot of the potential energy field close to the crack tip, with crack surfaces highlighted with "larger" atoms in red color. The mother (A), daughter (B) and granddaughter (C) cracks can be clearly identified.

The result suggests that shear dominated cracks along a bimaterial interface can reach the longitudinal wave speed of the stiffer material and can become supersonic with respect to the wave speeds of the soft material. Similar observations have been made in experiments. Rosakis *et al.* [96] reported crack speeds exceeding the longitudinal wave speed of the softer material and, at least on one occasion, reaching the longitudinal wave speed of the stiffer material. In another experimental study by Wu and Gupta [97], a crack at Nb-saphire interface was found to approach the longitudinal wave speed of the stiff material. Our results suggest three critical wave speeds for shear dominated interface cracks: the Rayleigh-wave speed of the soft material, the longitudinal wave

speed of the soft material and the longitudinal wave speed of the stiff material.

Atomistic studies are particularly suitable for studying the details of the processes close to the crack tip. Figure 39 shows a time sequence of the shear stress field very close to the crack tip during the nucleation of the secondary and tertiary cracks. The results suggest that a peak (concentration) in shear stress ahead of the crack causes nucleation of the daughter and granddaughter cracks. The shear stress peak ahead of the mother crack moves with the shear wave speed of the softer material (see Fig. 39, snapshot (2)). In Fig. 39, snapshot (3), the daughter crack has just nucleated, but there appears another peak in shear stress a few atomic spacings ahead of the daughter crack moving close to the shear wave speed of the stiffer material. In Fig. 39, snapshot (4), the granddaughter crack has appeared, as indicated by two shock fronts in the softer material. These observations are, at least qualitatively, in agreement with the mother-daughter mechanism observed for mode II cracks in homogeneous materials [31, 38]. The corresponding times of the snapshots are given in the caption of Fig. 39, and can be compared with the crack tip history and crack speed history shown in Figs. 34 and 35.

5.4 Discussion and conclusions: dynamics of interfacial cracks

The studies reported in this paper shows that cracking along a bimaterial interface is a rich phenomenon. We show that, barring hyperelastic effects, the limiting speed of an interfacial crack is the longitudinal wave speed of the stiffer material. A shear-dominated interface crack can propagate supersonically with respect to the softer material. We find that the crack speed changes discontinuously as the loading is increased, with more detailed analysis revealing a mother-daughter (tensile dominated loading) and mother-daughter-granddaughter mechanism (shear dominated loading) to achieve the ultimate limiting speed (see Figs. 25, 34 and 35). A clear jump in crack velocity can be observed when the daughter crack is nucleated. However, the nucleation of the granddaughter crack occurs with a more continuous velocity change.

A mother-daughter-granddaughter mechanism in shear dominated cracks has been reported in previous MD simulations of crack propagation along an interface between a harmonic material and an anharmonic material having the same elastic wave speeds under small deformation [13]. In the present study, we show that the mother-daughter-granddaughter mechanism not only occurs in nonlinear materials but also for linear elastic bimaterial interfaces. The fact that the mother-daughter-granddaughter mechanism occurs in both systems suggests that the phenomenon is robust and may occur under a wide range of conditions.

The elastic field of an interface crack can be very different from that of a homogeneous crack [98-101]. If crack propagation is supersonic with respect to one of the materials, multiple shock fronts are expected. The shock fronts shown in Figures 28, 29, 36-38 indicate that crack propagation is supersonic with respect to the soft material. A more detailed comparison of continuum theory and MD simulation is left to future work due to the known difficulties related to the oscillatory character of the continuum mechanics solutions.

We also simulated the dynamics of interfacial cracks with unconstrained crack branching under mode I dominated loading. The results of these studies are depicted in Figures 31 and 32. Figure 33 seems to reveal that there exists a tendency for cracks to branch off into the softer half space. This is in accord with observations made by other computational approaches at the continuum level by Xu and Needleman [91, 92]. However, we observe that if the constraint of interfacial crack motion is turned off *after* the secondary crack is nucleated, the crack maintains its supersonic speed without branching into either the soft or the stiff half space.

We find that the tendency to branch off into the soft material can not be explained by a difference in fracture surface energy. In a focused simulation study (case (iii)), we have adjusted the fracture surface energy so that it is equal in both the soft and the stiff regions and still observe a tendency of the crack to branch off into the soft region. This tendency of branching into the soft material may explain why supersonic cracking along interfaces has not been observed in experiments so far.

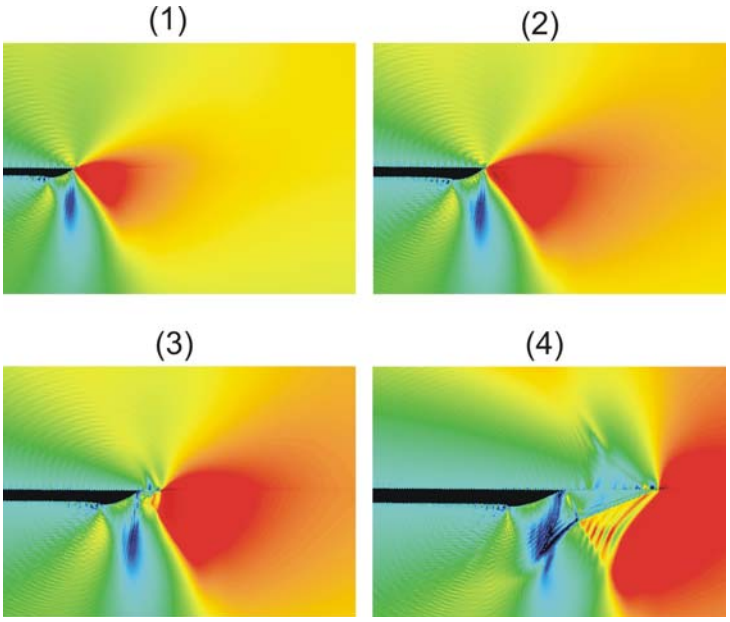

Fig. 39. Shear stress field during the transition from the mother crack (subplot (a)) to propagation of the granddaughter crack (see snapshot (1)). The analysis of the deformation field suggests that the large shear deformation ahead of the mother crack causes nucleation of the daughter crack. The peak in shear stress can be observed in snapshot (2), and appears by the dark red color. In snapshot (3), the daughter crack has nucleated, and there is still a peak shear stress ahead of the crack leading to initiation of the granddaughter crack (snapshot (4)). Here the granddaughter crack has appeared propagating at the longitudinal wave speed of the stiff material, while leaving two shock fronts in the soft material. Snapshots (1-4) are taken at times t=82.2, t=98.76, t=104.4, and t=115.2 respectively.

Our results suggest that successive generations of cracks via mother-daughter or mother-daughter-granddaughter mechanisms may be an important aspect of interface cracking. The detailed mechanisms should be subjected to more rigorous mathematical analysis and interpretations. This is left to a forthcoming article to be published elsewhere.

The present study illustrates that atomistic simulations can provide useful insights into the dynamics of crack propagation along

bimaterial interfaces. Combining large-scale atomistic simulations with continuum mechanics is a powerful approach in modern studies of dynamic fracture mechanics.

6. Summary and conclusion

We have presented a review of some of the recent results on large scale MD modelling of dynamic fracture. We have reported progresses in three areas of focus: (i) crack limiting speed, (ii) crack tip instabilities, and (iii) crack dynamics at interfaces.

The main conclusion is that hyperelasticity, the elasticity of large deformation, is crucial in order to form a clear picture of the failure process near a rapidly moving crack tip: Both the maximum crack speed and the dynamic instability are strongly influenced by the large-strain elastic properties. Phenomena such as intersonic mode I fracture (Figure 9) and supersonic mode II fracture (Figure 10) can not at all be addressed by classical, linear elastic theories. The observation of stable cracks in homogeneous materials at speeds beyond the Rayleigh-wave speed, as shown in Figure 23, can only be understood from a hyperelastic point of view. Further, we have shown that hyperelastic softening can significantly reduce the critical instability speed in cracks, as shown for instance in Figure 19. Classical linear elastic theories such as the Yoffe-model [78] fail when significant softening is present at the crack tip. Our new concept of a characteristic energy length scale χ helps to understand the relative significance of hyperelasticity in dynamic fracture (see Figure 13), both for the limiting speed of cracks (Figure 12) and for the instability dynamics (Figure 20).

Further, we find that interfaces and geometric confinement can play an important role in the dynamics of cracks. Crack propagation constrained along interfaces can significantly change the associated maximum speeds of crack motion. This is illustrated for instance by the studies using the concept of a weak fracture layer where the Rayleigh-wave speed of cracks can be attained by cracks (see Figure 6), versus the studies of cracks in homogeneous materials where the crack starts to wiggle at 73% of the theoretical limiting speed (see Figure 17). If cracks propagate along interfaces of elastically dissimilar materials, the

maximum crack speed can significantly change and new mechanisms of crack propagation such as daughter and granddaughter cracks appear, as illustrated in Figures 24, 32 and 33, leading to supersonic fracture relative to the soft material.

The results discussed in this article suggest that the definition of wave speeds according to the small-strain elastic properties is questionable in many cases, and a more complete picture of dynamic fracture should include local wave speeds near the cohesive failure of materials near a crack tip.

Acknowledgments

The simulations were carried out at the Garching Supercomputer Center of the Max Planck Society and at the MARS Linux cluster at the Max Planck Institute for Metals Research. We acknowledge continuing discussions with Dr. Farid F. Abraham on modeling dynamic fracture with molecular-dynamics simulations.

References

1. Field, J.E., *Brittle fracture-its study and application.* Contemp. Phys., 1971. **12**: p. 1-31.
2. Rice, J.R. and R.M. Thomson, *Ductile versus brittle behavior of crystals.* Phil. Mag., 1974. **29**: p. 73-97.
3. Argon, A., *Brittle to ductile transition in cleavage failure.* Acta Metall., 1987. **35**: p. 185-196.
4. Vashishta, P., R.K. Kalia, and A. Nakano, *Large-scale atomistic simulations of dynamic fracture.* Comp. in Science and Engrg., 1999: p. 56-65.
5. Kadau, K., T.C. Germann, and P.S. Lomdahl, *Large-Scale Molecular-Dynamics Simulation of 19 Billion particles.* Int. J. Mod. Phys. C, 2004. **15**: p. 193.
6. Buehler, M.J., et al., *The dynamical complexity of work-hardening: a large-scale molecular dynamics simulation.* Acta Mechanica Sinica, 2005. **21**(2): p. 103-111.
7. Zhou, S.J., et al., *Large-scale molecular-dynamics simulations of three-dimensional ductile failure.* Phys. Rev. Lett., 1997. **78**: p. 479-482.
8. Zhou, S.J., et al., *Large-scale molecular-dynamics simulations of dislocation interactions in copper.* Science, 1998. **279**: p. 1525-1527.

9. Buehler, M.J., et al., *Atomic Plasticity: Description and Analysis of a One-Billion Atom Simulation of Ductile Materials Failure.* Comp. Meth. in Appl. Mech. and Engrg., 2004.
10. Abraham, F.F., *How fast can cracks move? A research adventure in materials failure using millions of atoms and big computers.* Advances in Physics, 2003. **52**(8): p. 727-790.
11. Bulatov, V., et al., *Connecting atomistic and mesoscale simulations of crystal plasticity.* Nature, 1998. **391**: p. 669-672.
12. Abraham, F.F., et al., *Simulating materials failure by using up to one billion atoms and the world's fastest computer: Work-hardening.* P. Natl. Acad. Sci. USA, 2002. **99**(9): p. 5783-5787.
13. Abraham, F.F., et al., *Simulating materials failure by using up to one billion atoms and the world's fastest computer: Brittle Fracture.* P. Natl. Acad. Sci. USA, 2002. **99**(9): p. 5788-5792.
14. Freund, L.B., *Dynamic Fracture Mechanics*. 1990: Cambridge University Press, ISBN 0-521-30330-3.
15. Broberg, K.B., *Cracks and Fracture*. 1990: Academic Press.
16. Slepyan, L.I., *Models and Phenomena in Fracture Mechanics*. 2002: Springer, Berlin.
17. Cheung, K.S. and S. Yip, *A molecular-dynamics simulation of crack tip extension: the brittle-to-ductile transition.* Modelling Simul. Mater. Eng., 1993. **2**: p. 865-892.
18. Marder, M. and J. Fineberg, *How things break.* Phys. Today, 1996. **49**(9): p. 24-29.
19. Marder, M., *Molecular Dynamics of Cracks.* Computing in Science and Engineering, 1999. **1**(5): p. 48-55.
20. Holland, D. and M. Marder, *Ideal brittle fracture of silicon studied with molecular dynamics.* Phys. Rev. Lett., 1998. **80**(4): p. 746.
21. Ashurst, W.T. and W.G. Hoover, *Microscopic fracture studies in 2-dimensional triangular lattice.* Phys. Rev. B, 1976. **14**(4): p. 1465-1473.
22. Abraham, F.F., et al., *Instability dynamics of fracture: A computer simulation investigation.* Phys. Rev. Lett., 1994. **73**(2): p. 272-275.
23. Allen, M.P. and D.J. Tildesley, *Computer Simulation of Liquids*. 1989: Oxford University Press.
24. Abraham, F.F., et al., *A Molecular Dynamics Investigation of Rapid Fracture Mechanics.* J. Mech. Phys. Solids, 1997. **45**(9): p. 1595-1619.
25. Fineberg, J., et al., *Instability and dynamic fracture.* Phys. Rev. Lett., 1991. **67**(4): p. 457-460.
26. Marder, M. and S. Gross, *Origin of crack tip instabilities.* J. Mech. Phys. Solids, 1995. **43**(1): p. 1-48.

27. Sharma, A., R.K. Kalia, and P. Vashishta, *Large multidimensional data vizualization for materials science.* Comp. in Science and Engrg., 2003: p. 26-33.
28. Rountree, C.L., et al., *Atomistic aspects of crack propagation in brittle materials: Multimillion atom molecular dynamics simulations.* Annual Rev. of Materials Research, 2002. **32**: p. 377-400.
29. Buehler, M.J., F.F. Abraham, and H. Gao, *Stress and energy flow field near a rapidly propagating mode I crack.* Springer Lecture Notes in Computational Science and Engineering, 2004. **ISBN 3-540-21180-2**: p. 143-156.
30. Buehler, M.J., F.F. Abraham, and H. Gao, *Hyperelasticity governs dynamic fracture at a critical length scale.* Nature, 2003. **426**: p. 141-146.
31. Abraham, F.F. and H. Gao, *How fast can cracks propagate?* Phys. Rev. Lett., 2000. **84**(14): p. 3113-3116.
32. Swadener, J.G., M.I. Baskes, and M. Nastasi, *Molecular Dynamics Simulation of Brittle Fracture in Silicon.* Phys. Rev. Lett., 2002. **89**(8): p. 085503.
33. Li, J., et al., *Atomistic mechanisms governing elastic limit and incipient plasticity in crystals.* Nature, 2002. **418**: p. 307-309.
34. Cleri, F., et al., *Atomic-scale mechanism of crack-tip plasticity: Dislocation nucleation and crack-tip shielding.* Phys. Rev. Lett, 1997. **79**: p. 1309-1312.
35. Buehler, M.J., H. Gao, and Y. Huang, *Continuum and Atomistic Studies of a Suddenly Stopping Supersonic Crack.* Computational Materials Science, 2003. **28**(3-4): p. 385-408.
36. Gao, H., et al., *Flaw tolerant bulk and surface nanostructures of biological systems.* Mechanics & Chemistry of Biosystems, 2004. **1**(1): p. 37-52.
37. Buehler, M.J. and H. Gao, *A mother-daughter mechanism of supersonic crack growth of mode I dominated cracks at interfaces.* Accepted for publication in: Int. J. of Strength, Fracture and Complexity, 2005.
38. Gao, H., Y. Huang, and F.F. Abraham, *Continuum and atomistic studies of intersonic crack propagation.* J. Mech. Phys. Solids, 2001. **49**: p. 2113-2132.
39. Buehler, M.J. and H. Gao, *Dynamical fracture instabilities due to local hyperelasticity at crack tips.* under submission, 2005.
40. Abraham, F.F., et al., *Dynamic fracture of silicon: Concurrent simulation of quantum electrons, classical atoms, and the continuum solid.* MRS Bulletin, 2000. **25**(5): p. 27-32.
41. Abraham, F.F., et al., *Spanning the length scales in dynamic simulation.* Computers in Physics, 1998. **12**(6): p. 538-546.
42. Curtin, W.A. and R.E. Miller, *Atomistic/continuum coupling in computational materials science.* Modelling And Simulation In Materials Science And Engineering, 2003. **11**(3): p. R33-R68.
43. Shiari, B., R.E. Miller, and W.A. Curtin, *Coupled atomistic/discrete dislocation simulations of nanoindentation at finite temperature.* Journal Of Engineering

Materials And Technology-Transactions Of The Asme, 2005. **127**(4): p. 358-368.

44. Tadmor, E.B., M. Ortiz, and R. Phillips, *Quasicontinuum analysis of defects in solids.* Phil. Mag. A, 1996. **73**: p. 1529.
45. Shenoy, V., et al., *An Adaptive Methodology for Atomic Scale Mechanics - The Quasicontinuum Method.* J. Mech. Phys. Sol., 1999. **73**: p. 611-642.
46. Knap, J. and M. Ortiz, *An analysis of the quasicontinuum method.* J. Mech. Phys. Sol., 2001. **49**(9): p. 1899-1923.
47. Dupuy, L.M., et al., *Finite-temperature quasicontinuum: Molecular dynamics without all the atoms.* Physical Review Letters, 2005. **95**(6).
48. Wagner, G.J. and W.K. Liu, *Coupling of atomistic and continuum simulations using a bridging scale decomposition.* Journal Of Computational Physics, 2003. **190**(1): p. 249-274.
49. Plimpton, S., *Fast parallel algorithms for short-range molecular-dynamics.* Journal of Computational Physics, 1995. **117**: p. 1-19.
50. Vashishta, P., R.K. Kalia, and A. Nakano, *Multimillion atom molecular dynamics simulations of nanostructures on parallel computers.* Journal of Nanoparticle Research, 2003. **5**: p. 119-135.
51. Buehler, M.J. and H. Gao, *Ultra large scale atomistic simulations of dynamic fracture*. Handbook of Theoretical and Computational Nanotechnology, ed. W. Schommers and A. Rieth. 2006: American Scientific Publishers (ASP).
52. Abraham, F.F., *Computational statistical mechanics-methodology, applications and supercomputing.* Advances in Physics, 1986. **35**(1): p. 1-111.
53. Chenoweth, K., et al., *Simulations on the thermal decomposition of a poly(dimethylsiloxane) polymer using the ReaxFF reactive force field.* Journal Of The American Chemical Society, 2005. **127**(19): p. 7192-7202.
54. Ercolessi, F. and J.B. Adams, *Interatomic potentials from 1st principle-calculations - the force matching method.* Europhys. Lett., 1994. **28**(8): p. 583-588.
55. Baskes, M.I., *Determination of modified embedded atom method parameters for nickel.* Materials Chemistry and Physics, 1997. **50**(2): p. 152-158.
56. Abraham, F.F., *Dynamics of brittle fracture with variable elasticity.* Phys. Rev. Lett., 1996. **77**(5): p. 869.
57. Abraham, F.F., et al., *Ab-initio dynamics of rapid fracture.* Modelling Simul. Mater. Sci. Eng., 1998. **6**: p. 639-670.
58. Abraham, F.F. and H. Gao, *Anamalous Brittle-Ductile Fracture Behaviors in FCC Crystals.* Phil. Mag. Lett., 1998. **78**: p. 307-312.
59. Washabaugh, P.D. and W.G. Knauss, *A reconcilation of dynamic crack velocity and Rayleigh-wave speed in isotropic brittle solids.* Int. J. Fracture, 1994. **65**: p. 97-114.
60. Buehler, M.J. and H. Gao, *Dynamical fracture instabilities due to local hyperelasticity at crack tips.* Accepted for publication in: Nature.

61. Buehler, M.J. and H. Gao, *Biegen und Brechen im Supercomputer.* Physik in unserer Zeit, 2004. **35**(1).
62. Gao, H., *A theory of local limiting speed in dynamic fracture.* J. Mech. Phys. Solids, 1996. **44**(9): p. 1453-1474.
63. Gao, H., *Elastic waves in a hyperelastic solid near its plane-strain equibiaxial cohesive limit.* Philosphical Magazine Letters, 1997. **76**(5): p. 307-314.
64. Fineberg, J., et al., *Instability in the propagation of fast cracks.* Phys. Rev. B, 1992. **45**(10): p. 5146-5154.
65. Sharon, E. and J. Fineberg, *Confirming the continuum theory of dynamic brittle fracture for fast cracks.* Nature, 1999. **397**: p. 333.
66. Buehler, M.J., *Atomistic simulations of brittle fracture and deformation of ultra thin copper films*, in *Chemistry*. 2004, University of Stuttgart: Stuttgart.
67. Tsai, D.H., *Virial theorem and stress calculation in molecular-dynamics.* J. of Chemical Physics, 1979. **70**(3): p. 1375-1382.
68. Zhou, M., *Equivalent continuum for dynamically deforming atomistic particle systems.* Phil. Mag. A, 2002. **82**(13).
69. Zimmermann, J.A., *Continuum and atomistic modeling of dislocation nucleation at crystal surface ledges*. 1999, Stanford University.
70. Buehler, M.J., H. Gao, and Y. Huang, *Continuum and Atomistic Studies of the Near-Crack Field of a rapidly propagating crack in a Harmonic Lattice.* Theoretical and Applied Fracture Mechanics, 2004. **41**: p. 21-42.
71. Buehler, M.J., A. Hartmaier, and H.J. Gao, *Atomistic and continuum studies of crack-like diffusion wedges and associated dislocation mechanisms in thin films on substrates.* Journal Of The Mechanics And Physics Of Solids, 2003. **51**(11-12): p. 2105-2125.
72. Griffith, A.A., *The phenomenon of rupture and flows in solids.* Phil. Trans. Roy. Soc. A, 1920. **221**: p. 163-198.
73. Broberg, K.B., *Dynamic crack propagation in a layer.* Int. J. Solids Struct., 1995. **32**(6-7): p. 883-896.
74. Cramer, T., A. Wanner, and P. Gumbsch, *Energy dissipation and path instabilities in dynamic fracture of silicon single crystals.* Phys. Rev. Lett., 2000. **85**: p. 788-791.
75. Cramer, T., A. Wanner, and P. Gumbsch, *Crack Velocities during Dynamic Fracture of Glass and Single Crystalline Silicon.* Phys. Status Solidi A, 1997. **164**: p. R5.
76. Gumbsch, P., S.J. Zhou, and B.L. Holian, *Molecular dynamics investigation of dynamic crack instability.* Phys. Rev. B, 1997. **55**: p. 3445.
77. Deegan, R.D., et al., *Wavy and rough cracks in silicon.* Phys. Rev. E, 2003. **67**(6): p. 066209.
78. Yoffe, E.H., *The moving Griffith crack.* Phil. Mag., 1951. **42**: p. 739-750.
79. Petersan, P.J., et al., *Cracks in rubber under tension break the shear wave speed limit.* Phys. Rev. Letters, 2004. **93**: p. 015504.

80. Gao, H., *Surface roughening and branching instabilities in dynamic fracture.* J. Mech. Phys. Solids, 1993. **41**(3): p. 457-486.
81. Eshelby, J.D., *Elastic field of a crack extending non-uniformly under general anti-planbe loading.* J. Mech. Phys. Solids, 1969. **17**(3): p. 177-199.
82. Freund, L.B., *Crack propagation in an elastic solid subjected to general loading, II. Nonuniform rate of extension.* J. Mech. Phys. Solids, 1972. **20**: p. 141-152.
83. Abraham, F.F., *Unstable crack motion is predictable.* Advances in Physics, 2005. **53**: p. 1071-1078.
84. Heizler, S.I., D.A. Kessler, and H. Levine, *Mode I fracture in a nonlinear lattice with viscoelastic forces.* Phys. Rev. E, 2002. **6**: p. 016126.
85. Buehler, M.J., et al., *The Computational Materials Design Facility (CMDF): A powerful framework for multiparadigm multi-scale simulations.* Mat. Res. Soc. Proceedings, 2006. **894**: p. LL3.8.
86. Buehler, M.J., A.C.T.v. Duin, and W.A. Goddard, *Multi-paradigm multi-scale modeling of dynamical crack propagation in silicon using the ReaxFF reactive force field.* Submitted for publication to Phys. Rev. Lett., 2005.
87. Buehler, M.J., A.C.T.v. Duin, and W.A. Goddard, *Multi-paradigm multi-scale modeling of dynamical crack propagation in silicon using the ReaxFF reactive force field.* Mat. Res. Soc. Proceedings 904E, 2006: p. BB4.28.
88. Tersoff, J., *Empirical interatomic potentials for carbon, with applications to amorphous carbon.* Phys. Rev. Lett., 1988. **61**(25): p. 2879-2883.
89. Duin, A.C.T.v., et al., *ReaxFF SiO: Reactive Force Field for Silicon and Silicon Oxide Systems.* J. Phys. Chem. A, 2003. **107**: p. 3803-3811.
90. Buehler, M.J. and H. Gao, *A mother-daughter-granddaughter mechanism of supersonic crack growth of shear dominated intersonic crack motion along interfaces of dissimilar materials.* Journal of the Chinese Institute of Engineers, 2004. **27**(6): p. 763-769.
91. Xu, X.P. and A. Needleman, *Numerical simulations of dynamic interfacial crack growth allowing for crack growth away from the bond line.* International Journal of Fracture, 1996. **74**(3): p. 253-275.
92. Xu, X.P. and A. Needleman, *Numerical simulations of dynamic crack growth along an interface.* International Journal of Fracture, 1996. **74**(4): p. 289-324.
93. Rosakis, A.J., O. Samudrala, and D. Coker, *Cracks faster than the shear wave speed.* Science, 1999. **284**(5418): p. 1337-1340.
94. Burridge, R., *Admissible speeds for plain-strain self-similar cracks with friction but lacking cohesion.* Geophys. J. Roy. Astron. Soc., 1973. **35**: p. 439-455.
95. Andrews, D.J., *Rupture velocity of plane strain shear cracks.* J. Geophys. Res., 1976. **81**: p. 5679-5687.
96. Rosakis, A.J., *Intersonic crack propagation in bimaterial systems.* J. Mech. Phys. Solids, 1998. **6**(10): p. 1789-1813.

97. Wu, J.X. and V. Gupta, *Observations of Transonic Crack Velocity at a Metal/Ceramic Interface.* Journal of the Mechanics and Physics of Solids, 2000. **48**(3): p. 609-619.
98. Zak, A.R. and M.L. Williams, *Crack point singularities at a bi-material interface.* J. Appl. Mech., 1963. **30**: p. 142-143.
99. Williams, M.L., *The stresses areound a fault or crack in dissimilar media.* Bull. Seismol. Soc. America, 1959. **49**: p. 199-204.
100. Liu, C., J. Lambros, and A.J. Rosakis, *Highly transient elastodynamic crack growth in a bimaterial interface: higher order asymptotic analysis and experiments.* J. Mech. Phys. Solids, 1993. **41**: p. 1887-1954.
101. Liu, C., Y. Huang, and A.J. Rosakis, *Shear dominated transonic interfacial crack growth in a bimaterial-II. Asymptotic fields and favorable velocity regimes.* J. Mech. Phys. Solids, 1993. **43**(2): p. 189-206.